Universidade de Aveiro
2023

DIOGO DE ASSIS MAGALHÃES MALHEIRO

SOLITÕES QUÁRTICOS DISSIPATIVOS EM LASERS DE FIBRA COM MODOS BLOQUEADOS

DISSIPATIVE QUARTIC SOLITONS IN MODE-LOCKED FIBER LASERS

Universidade de Aveiro
2023

DIOGO DE ASSIS MAGALHÃES MALHEIRO

SOLITÕES QUÁRTICOS DISSIPATIVOS EM LASERS DE FIBRA COM MODOS BLOQUEADOS

DISSIPATIVE QUARTIC SOLITONS IN MODE-LOCKED FIBER LASERS

Dissertação apresentada à Universidade de Aveiro para cumprimento dos requisitos necessários à obtenção do grau de Mestre em Engenharia Física, realizada sob a orientação científica da Doutora Margarida Maria Resende Vieira Facão, Professora auxiliar do Departamento de Física da Universidade de Aveiro, e da Doutora Maria Inês Barbosa de Carvalho, Professora associada da Faculdade de Engenharia da Universidade do Porto.

Este trabalho foi desenvolvido no âmbito de projetos financiados por fundos nacionais através da FCT/MEC, nomeadamente, UIDB/50025/2020, UIDP/50025/2020, LA/P/0037/2020 e UIDB/50014/2020

o júri / the jury

presidente / president	Prof. Doutor Luís Miguel Rino Cerveira da Silva professor auxiliar do Departamento de Física da Universidade de Aveiro
arguente / examiner	Prof. Doutor Augusto da Silveira Rodrigues professor auxiliar da Faculdade de Ciências da Universidade do Porto
orientadora / supervisor	Prof. Doutora Margarida Maria Resende Vieira Facão professora auxiliar do Departamento de Física da Universidade de Aveiro

agradecimentos / acknowledgements

Quero começar por agradecer às minhas orientadoras, a professora Margarida Facão e a professora Maria Inês Carvalho, por todo o incansável apoio, pelos conselhos, pelas aprendizagens e pelas longas conversas e discussões que me fizeram sentir que o trabalho aqui desenvolvido foi um real esforço de equipa.
Ao Departamento de Física da Universidade de Aveiro, ao I3N, ao INESC TEC e à FCT pelo financiamento dentro dos projetos UIDB/50025/2020, UIDP/50025/2020, LA/P/0037/2020 e UIBD/50014/2020 que permitiram a minha participação no *Extreme Waves International Workshop* em Dresden.
À minha família por todo o apoio ao longo da minha jornada académica.
Aos meus amigos e colegas com quem, ao longo dos últimos 5 anos, partilhei não só muitos desabafos e momentos de desespero académico mas também muitas gargalhadas, quer fosse nas cartas, no bilhar ou no padel, que tornaram este difícil percurso muito menos solitário.
Por último, mas não menos importante, agradeço ao Hélder, pela companhia, pelo apoio incondicional e pela força que me dás todos os dias.
A todos e todas, o meu mais sincero obrigado!

Palavras Chave

solitões quárticos, modelo distribuído, relação energia-largura, solitões dissipativos, lasers de modos bloqueados

Resumo

Os solitões quárticos têm ganho bastante atenção nos últimos anos uma vez que a sua energia depende inversamente da largura temporal ao cubo. Esta relação é muito útil para aplicações onde são necessários impulsos curtos altamente energéticos, como na geração de supercontínuo e de pentes óticos de frequência. Apesar dos solitões quárticos terem sido bastante estudados em modelos conservativos, ainda não é claro se a relação energia-largura mencionada é universalmente válida em modelos dissipativos.

Nesta dissertação, visando um estudo mais aprofundado dessa relação e a procura de métodos para maximizar a energia dos impulsos, um laser em fibra com bloqueio de modos passivo foi simulado numericamente a partir de um modelo distribuído que inclui um termo de dispersão de quarta ordem (D4O). Encontraram-se soluções localizadas utilizando o método dos gradientes conjugados de Newton, a sua propagação foi simulada recorrendo a um método pseudo-espetral e a estabilidade das soluções foi analisada através do cálculo dos valores próprios do operador linear de estabilidade.

Obtiveram-se soluções do tipo solitão quártico para D4O positiva e negativa, na presença ou na ausência de dispersão de segunda ordem de qualquer sinal. Sob uma filtragem espetral fraca, com D4O negativa as soluções são do tipo impulso Gaussiano com oscilações nas caudas, tomando a forma de secantes hiperbólicas sobre um pedestal mais largo cujas caudas decaem exponencialmente com D4O positiva. Sob filtragem espetral forte, todas as soluções tomaram a forma de secantes hiperbólicas. Em todos os casos, as soluções tinham um perfil de fase não-uniforme e os impulsos têm, por isso, trinado.

Os termos de ganho, potência de saturação e de filtragem espetral foram variados para estudar a dependência da energia e da larguram com estes parâmetros. Com D4O negativa, a energia aumenta com o inverso da largura ao cubo, sob filtragem espetral fraca. Quando este último parâmetro ultrapassa um valor limiar, a energia começa a crescer com a largura. Para D4O positiva, a energia depende sempre inversamente da largura, mas não foi encontrada nenhuma relação matemática que descrevesse claramente esta dependência para os três varrimentos. De qualquer das formas, verificou-se que a energia era superior e a largura inferior no regime de D4O negativa.

Finalmente, a análise de estabilidade mostrou que a energia dos impulsos pode ser maximizada diminuindo o termo de filtragem espetral. Escolhendo valores de ganho e de potência de saturação que garantam a estabilidade das soluções, e considerando D4O negativa, obtiveram-se solitões quárticos com larguras de 39 fs e energias de 391 nJ

Keywords

quartic solitons, distributed model, energy-width scaling, dissipative solitons, mode-locked lasers.

Abstract

Quartic solitons have garnered much attention in recent years, due to their energy scaling with the inverse of the third power of the width. This is of great importance in applications such as supercontinuum and frequency comb generation, where highly energetic ultrashort pulses are required. Although quartic solitons have been the subject of much study in conservative models, more research is required to establish the universal validity of the aforementioned energy-width scaling in dissipative models.

In this dissertation, aiming to study this energy-width relation further and to find ways to maximize pulse energy, a passively mode-locked fiber laser was numerically simulated using a distributed model including a fourth-order dispersion (4OD) term. Localized solutions were found using the Newton conjugate-gradient method, their propagation was simulated through a pseudo-spectral method and the stability of the solutions was analysed by calculating the eigenvalues of the linear stability operator.

Quartic soliton solutions were found for positive and negative 4OD, in the presence or in the absence of second order dispersion, regardless of its sign. Under weak spectral filtering, Gaussian pulses with oscillating tails were found for negative 4OD, and hyperbolic secant pulses sitting upon a broad pedestal with exponentially decaying tails were found for positive 4OD. Under strong filtering, pulses take the shape of hyperbolic secant curves. In all cases, the solutions have a non-uniform phase profile and are therefore chirped.

The gain, saturation power and spectral filtering parameters were swept to study the energy and width dependence on these parameters. For negative 4OD, the energy scaled inversely with the third power of the width under weak filtering. When the spectral filter parameter increases beyond a threshold, the energy starts increasing with the width. For positive 4OD, the energy always scaled inversely with the width, but no clear mathematical trend was found that could describe the behaviour of the curves for each parameter sweep. Nevertheless, the energy was found to be greater and pulse widths to be shorter in the negative 4OD regime.

Finally, the stability analysis showed that the pulse energy can be maximized by lowering the spectral filtering term. Setting the gain and the saturation power to values that ensure the stability of the solutions, and considering negative 4OD, yielded quartic solitons as short as 39 fs and with energies of 391 nJ.

Contents

List of Acronyms **i**

List of Symbols **ii**

List of Figures **iv**

1 Introduction **1**
- 1.1 Motivation and Framework . . . 1
- 1.2 Objectives and Outline . . . 4
- 1.3 Contributions . . . 5

2 Conservative and Dissipative Solitons **6**
- 2.1 Dispersion and Nonlinear Effects . . . 6
  - 2.1.1 Dispersion . . . 6
  - 2.1.2 Nonlinearity . . . 8
- 2.2 The Nonlinear Schrödinger Equation . . . 9
- 2.3 Dissipative Solitons in Mode-Locked Lasers . . . 12

3 Numerical Methods **17**
- 3.1 Newton Conjugate Gradient Method . . . 18
- 3.2 Pseudo-spectral Method . . . 23
- 3.3 Linear Stability Analysis . . . 25

4 Results and Discussion **28**
- 4.1 Quartic Soliton Solutions of the Distributed Model . . . 28
- 4.2 Energy-Width Scaling . . . 34
- 4.3 Energy Maximization . . . 38

5 Conclusions and Future Work **42**

References **44**

List of Acronyms

2OD second order dispersion

3OD third order dispersion

4OD fourth order dispersion

CG conjugate-gradient

CGLE complex Ginzburg-Landau equation

FT Fourier transform

FWHM full width at half maximum

GVD group velocity dispersion

NCG Newton conjugate-gradient

NLSE nonlinear Schrödinger equation

OC output coupler

ODE ordinary differential equation

PDE partial differential equation

PQS pure-quartic soliton

RK4 fourth-order Runge-Kutta

SA saturable absorber

SPM self-phase modulation

List of Symbols

β	mode propagation constant
β_1	inverse group velocity
β_2	second order dispersion parameter
β_4	fourth order dispersion parameter
β_m	m-th order dispersion parameter
γ	nonlinear parameter
$\bar{\gamma}$	effective nonlinear parameter
δ	linear loss
$\delta\omega$	frequency chirp
ε	nonlinear gain
ε_0	vaccum permitivity
ζ	spectral filtering
η	small perturbation
λ	stability eigenvalues
λ_0	wavelength
μ	nonlinear gain saturation
ν	Kerr effect saturation parameter
σ	propagation constant shift
ϕ	phase
$\chi^{(j)}$	j-th order susceptibility
ω	frequency
ω_0	central frequency
A_{eff}	effective mode area
c	vacuum speed of light
$\mathbf{d}_n$	n-th conjugate direction
D_2	normalized second order dispersion paramenter
D_4	normalized fourth order dispersion parameter
$\mathbf{D}$	dispersion operator
E	energy
E_{sat}	gain saturation energy
$\mathbf{E}$	electric filed
g	saturated gain
g_0	small-signal gain
h	step size
k_{OC}	loss at the output coupler
L	waveguide/cavity length
L_{2OD}	dispersion length
L_{NL}	nonlinear length
L_{SA}	saturable absorber length
$\mathbf{L}_1$	linearization operator of function $\mathbf{L}_0(\mathbf{u})$
M	modulation depth
$\mathbf{M}$	preconditioning matrix
n	reffractive index
n_2	Kerr coefficient
n_{core}	core reffractive index
n_{clad}	cladding reffractive index
n_{eff}	effective reffractive index

P_{peak}	peak power
P_{sat}	saturation power
$\bar{P}_{\mathrm{sat}}$	effective saturation power
$\mathbf{P}$	polarization
q	normalized slowly varying pulse envelope
r_i	i-th increment function
$\mathbf{r}_n$	n-th residual
t	retarded time
T	normalized retarded time
T_0	initial pulse width
T_2	inverse linewidth of the parabolic gain
$\mathcal{T}$	saturable absorber transmittance
u	real temporal profile
U	complex temporal profile
v_g	group velocity
v_{g_0}	group velocity at the central frequency
w_0	width
W	slowly varying pulse envelope
z	propagation coordinate
Z	normalized propagation distance

List of Figures

1.1 Energy-width scaling of pure-quartic solitons (PQSs) following [39] with $\beta_4 = -0.08$ ps^{4}m^{-1} and $\gamma = 0.005$ W^{-1}m^{-1} (blue line), conventional solitons [3] with $\beta_2 = -0.024$ ps^{2}m^{-1} and the same γ (red dashed line) and of quartic solitons with positive fourth order dispersion (4OD), approximated from the results in [46]. 4

2.1 An optical pulse propagating through a dispersive medium, being broadened as result of the frequency dependence of the group velocity. In the depicted case, the low (red, denoted "R") frequency components travel faster than the high (blue, denoted "B") frequency component. Adapted from [53] 6
2.2 Frequency dependence of the inverse group velocity for pulses traveling in dispersive media with pure (a) even-order or (b) odd-order dispersion. 8
2.3 Schematic representation of soliton formation from the interplay of self-phase modulation (SPM) and anomalous group velocity dispersion (GVD). SPM induces a red-shift on the leading edge and a blue-shift on the trailing edge of the pulse, both of which tend to the center of the pulse through the action of negative even order dispersion. Adapted from [4]. 11
2.4 Qualitative differences of the impact of equation parameters on soliton solutions of conservative and dissipative systems. In the former case, dispersion and nonlinear parameters define a family of solution while in the latter, the introduction of gain and loss parameters yield a single solution. Adapted from [5]. 13
2.5 A simple mode-locked fiber laser scheme made up of a doped fiber amplifier, a semiconductor saturable absorber (SA), and an output coupler (OC). Not illustrated is the optical pumping required for laser operation, achieved through either a diode laser array or another fiber laser. Adapted from [68]. 14

3.1 Dependence of the normalized peak power on dZ. As dZ decreases, the peak power tends to a constant value, marked by the black dashed line. Parameters: $\beta_2 = 0$, $\beta_4 = -0.080$ ps^{4}m^{-1}, $g_0 = 1.461$ m^{-1}, $P_{\text{sat}} = 83.3$ W, $T_2 = 100$ fs. . . 24
3.2 (a) Linear stability operator spectrum of the solution of Eq. (3.2) obtained with $\beta_2 = 0$, $\beta_4 = -0.080$ ps^{4}m^{-1}, $g_0 = 1.50$ m^{-1}, $T_2 = 100$ fs, $P_{\text{sat}} = 80$ W. The eigenvalues with negative imaginary parts are evidence that this particular solution is unstable, as shown by the erratic oscillations in the peak power in (b). 27

4.1 Pulse profiles in (a) linear and (b) logarithmic scale for $\beta_4 = \pm 0.080$ and 0 ps^{4}m^{-1}. Note that in (a), the left-hand side axis refers to the pulse with $\beta_4 < 0$ and the right-hand side axis refers to the remaining ones. The inset highlights the oscillations in the tails of the solution with $\beta_4 < 0$. Parameters: $\beta_2 = -0.024$ ps^{2}m^{-1}, $g_0 = 1.45$ m^{-1}, $T_2 = 100$ fs and $P_{\text{sat}} = 80$ W. 28
4.2 Pulse profiles for negative, zero and positive β_2, for (a) $\beta_4 = -0.080$ ps^{4}m^{-1}, $g_0 = 1.40$ m^{-1}, $T_2 = 100$ fs and $P_{\text{sat}} = 80$ W; and (b) $\beta_4 = -0.080$ ps^{4}m^{-1}, $T_2 = 110$ fs, $P_{\text{sat}} = 80$ W and $g_0 = 1.45$ m^{-1} when $\beta_2 \leq 0$ and $g_0 = 1.46$ m^{-1} for $\beta_2 > 0$. In all non-vanishing cases, $|\beta_2| = 0.024$ ps^{2}m^{-1}. 29

4.3 Phase profiles (top row) and chirp (bottom row) of soliton solutions with (a) and (d) $\beta_4 = -0.080$ ps^{4}m^{-1}; (b) and (e) $\beta_4 = 0$ and (c) and (f) $\beta_4 = 0.080$ ps^{4}m^{-1}. Parameters: $\beta_2 = -0.024$ ps^{2}m^{-1}, $g_0 = 1.45$ m^{-1}, $T_2 = 100$ fs and $P_{\text{sat}} = 80$ W. 30

4.4 Pulse spectra in (a) linear and (b) logarithmic scale for $\beta_4 = \pm 0.080$ and 0 ps^{4}m^{-1}. Parameters: $\beta_2 = -0.024$ ps^{2}m^{-1}, $g_0 = 1.45$ m^{-1}, $T_2 = 100$ fs and $P_{\text{sat}} = 80$ W. 31

4.5 Pulse shapes for different values of T_2 for (a), (b) $\beta_4 = -0.080$ ps^{4}m^{-1}, $P_{\text{sat}} = 3$ W and $g_0 = 1.36$ m^{-1}, and (c), (d) $\beta_4 = 0.080$ ps^{4}m^{-1}, $P_{\text{sat}} = 80$ W and $g_0 = 1.48$ m^{-1}, in linear and logarithmic scale, respectively. In both cases, $\beta_2 = 0$. 32

4.6 (a), (c) Phase profiles and (b), (d) chirp of the pulses for different values of T_2, for $\beta_4 = -0.080$ ps^{4}m^{-1}, $P_{\text{sat}} = 3$ W and $g_0 = 1.36$ m^{-1} (top row) and $\beta_4 = 0.080$ ps^{4}m^{-1}, $P_{\text{sat}} = 80$ W and $g_0 = 1.48$ m^{-1} (bottom row). In all cases, $\beta_2 = 0$. 33

4.7 Pulse spectra for varying T_2 in (a), (c) linear and (b), (d) logarithmic scale, for negative (top row) and positive (bottom row) fourth order dispersion (4OD). Parameters: $\beta_2 = 0$, $\beta_4 = \pm 0.080$ ps^{4}m^{-1}, $g_0 = 1.36$ m^{-1}, $P_{\text{sat}} = 3$ W. 34

4.8 Energy and width dependence on the fourth order dispersion (4OD) parameter. (a) Energy dependence with β_4. (b) Width dependence with β_4. The inset highlights the depencence of the width with negative fourth order dispersion (4OD). (c) Energy-width curve when β_4 is swept from negative to positive values. Parameters: $\beta_2 = -0.024$ ps^{2}m^{-1}, $g_0 = 1.45$m^{-1}, $T_2 = 100$ fs and $P_{\text{sat}} = 80$ W 35

4.9 Energy dependence with g_0 (left column), P_{sat} (middle column) and T_2 (right column) for $\beta_4 = -0.080$ ps^{4}m^{-1} (top row) and $\beta_4 = 0.080$ ps^{4}m^{-1} (bottom row). When kept constant, $P_{\text{sat}} = 80$ W and $T_2 = 100$ fs for either fourth order dispersion (4OD) value, while g_0 took values of 1.36 m^{-1} when $\beta_4 < 0$ and of 1.45 m^{-1} when $\beta_4 > 0$. 36

4.10 Width dependence with g_0 (left column), P_{sat} (middle column) and T_2 (right column) for $\beta_4 = -0.080$ ps^{4}m^{-1} (top row) and $\beta_4 = 0.080$ ps^{4}m^{-1} (bottom row). When kept constant, $P_{\text{sat}} = 80$ W and $T_2 = 100$ fs for either fourth order dispersion (4OD) value, while g_0 took values of 1.36 m^{-1} when $\beta_4 < 0$ and of 1.45 m^{-1} when $\beta_4 > 0$. 37

4.11 Energy-width curves using $\log_{10}$ scale and associated fittings, obtained by sweeping g_0, P_{sat} and T_2 for (a) $\beta_4 = -0.080$ ps^{4}m^{-1} and (b). When kept constant, $T_2 = 100$ fs, $g_0 = 1.36$ m^{-1} for $\beta_4 < 0$ and 1.45 m^{-1} for $\beta_4 > 0$ and when not specified, $P_{\text{sat}} = 80$ W. 38

4.12 Region of existence of stable solitons in the $g_0 - T_2$ plane. In the colored regions, solutions exist and propagate steadily. The base 10 logarithm of the energies in nJ ((a) and (c)) and the widths in fs ((a) and (b)) are represented as contour plots, for $P_{\text{sat}} = 80$ W (top row) and $P_{\text{sat}} = 160$ W (bottom row). For each saturation power, the insets show the highest energy pulses found within the stability border, displaying the corresponding energy and width values. Dispersion parameters: $\beta_2 = 0$, $\beta_4 = -0.08$ ps^{4}m^{-1}. 40

4.13 Region of existence of stable solitons in the $g_0 - T_2$ plane. The energy in pJ (a) and the width in ps (b) are represented above the curves as contour plots. Equation parameters: $\beta_2 = 0$, $\beta_4 = 0.08$ ps^{4}m^{-1} and $P_{\text{sat}} = 80$ W. 41

1. Introduction

The first chapter of this manuscript provides an introduction to this dissertation. Section 1.1 contains the motivation as well as the contextualizing framework. Section 1.2 presents the main goals and outlines the present document. Section 1.3 lists the contributions made from the development of this work.

1.1 Motivation and Framework

In 1834, in the Glasgow-Edinburgh union canal, J. S. Russel observed a wave that traveled through the canal undisturbed. Russell followed its propagation on horseback for a few kilometers until the wave eventually decayed. These kinds of waves were then referred to as *solitary waves* [1]. The term *soliton* was first introduced by Zabusky and Kruskal in 1965 [2] after numerically observing collisions of two solitary-wave pulses propagating in a nonlinear dispersive medium. Upon the collision, the pulses overlapped and interacted nonlinearly. In the moments succeeding the interaction, the pulses reappeared, with their shape and size being kept intact. Following these observations, the authors concluded that these solitary pulses - solitons - interact through a nonlinear physical process without scattering irreversibly. Solitons, in conservative media where energy transfer mechanisms between the pulse and the media are not present, can be defined as localized wave structures that arise from the balance of dispersion/diffraction and nonlinearity, leading to waves that maintain their shape and velocity during propagation [3–5]. It is important to stress that both spatial and temporal solitons exist but in this work, the focus lies on temporal solitons. Therefore, by omission, whenever solitons are referred to, it is implied that temporal solitons are being discussed.

Ever since their discovery, solitons have been the subject of study in many scientific fields, such as hydrodynamics [6], biological [7] and atmospheric systems [8], plasma physics [2], Bose-Einstein condensates [9] and astrophysics [10]. In the field of optics, solitons garnered much attention since they were first theoretically demonstrated in optical fibers with anomalous group velocity dispersion (GVD) by Hasegawa and Tappert in 1973 [11], being first experimentally demonstrated in 1980 by Mollenauer *et al.* [12]. During the 1990s, optical solitons were the subject of much interest in optical communications [13], but the need for careful management of fiber nonlinearity, gain and loss [14] eventually overthrew the potential advantages soliton communication systems could have, rendering them impractical [4].

In the field of mode-locked lasers, soliton effects have been exploited to generate ultrashort pulses with widths well below 100 fs [15, 16]. The generation of such short pulses is important in many fields such as chemistry [17], materials science [18], optical communications [19], medicine and biology [20], among others. Since mode-locked lasers are non-conservative media, solitons in these systems arise not only from the balance of dispersion with non linearity but also between the balance of gain and loss mechanisms. These solitons are therefore referred to as *dissipative solitons* [5].

Soliton based lasers have the advantage of the soliton energy, E, being inversely proportional to the temporal width, w_0 [3]. Therefore, they have the capability of generating ultrashort pulses with high energies [21], which are useful in the context of nonlinear biomedical imaging [22] and material processing [4] as well as supercontinuum [23, 24] and frequency comb generation [25].

Even though most work in this field, has been mainly focused on solitons, conservative or otherwise, arising from the interplay between the Kerr effect and second order dispersion (2OD) (generally known as *conventional solitons*), the effects of higher-orders of dispersion on soliton formation have been historically studied. In 1988, Blow *et al.* [26] considered third order dispersion (3OD) and fourth order dispersion (4OD) as perturbations to soliton formation and propagation, with the former dispersion term leading to a loss in symmetry and the latter to pulse breakup. In 1993, Haus *et al.* [27] theoretically studied the effect of 3OD in the context of mode-locked lasers, finding that it leads to an increase in pulse width and radiation losses while Höök and Karlsson [28] reported that in optical fibers, at the minimum-dispersion wavelength, 4OD leads to dispersive radiation and to the decay of solitons. In 1994, Kodama *et al.* [29] studied the impact of 3OD on soliton stability and thus, up until this point, higher orders of dispersion were generally seen as detrimental. However, in the same year, Karlsson and Höök [30] found a family of sech^2 shaped solitons occurring in media with negative 2OD and 4OD and in the absence of 3OD (later included by Kruglov and Harvey [31]), defined as,

$$W(t,z) = 3\sqrt{\frac{\beta_2^2}{5|\beta_4|}}\mathrm{sech}^2\left(\sqrt{\frac{3\beta_2}{\beta_4}}t\right)\exp\left(i\frac{24\beta_2^2}{25|\beta_4|}z\right), \tag{1.1}$$

where W is the slowly varying pulse envelope, t is the retarded time in the frame of reference of the pulse, z is the propagation distance and β_2 and β_4 are the 2OD and 4OD parameters, respectively. Moreover, Akhmediev *et al.* [32] reported soliton solutions with oscillating tails in the presence of 4OD and Christov *et al.* [33] found stationary pulses in numerical simulations of a Ti:sapphire mode-locked laser in the presence of 2OD and 4OD. In 1995, Buryak and Akhmediev [34] investigated multisoliton bound states in optical fibers with 4OD, and established that such states were stable if the second derivative of the Hamiltonian-energy curve at the point of interest is positive, while in 1996, Piché *et al.* [35] found an analytical expression for bright optical solitons in the presence of 4OD and that these solutions were stable in the presence of 3OD as well, as long as the former parameter does not exceed a threshold value. This collection of works opened the chapter of solitons in media with 4OD, henceforth referred to as *quartic solitons.*

Research interest in quartic solitons has grown over the last decade. In 2013, Roy and Biancalana [36] theoretically explored quartic solitons in silicon-based slot waveguides, in the presence of negative 2OD and 4OD. In 2016, Blanco-Redondo *et al.* [37] coined the term pure-quartic solitons (PQSs) when the authors theoretically and experimentally demonstrated a class of solitons arising only from the interaction of negative 4OD and Kerr nonlinearities, with small 2OD and 3OD terms. The authors also demonstrated that quartic solitons survive even when $\beta_2 > 0$, and that the energy of PQSs scales with w_0^{-3}, as compared to the w_0^{-1}

scaling found in conventional solitons. Following this work, in 2018, Lo *et al.* [38] developed a numerical analysis to aid the design of microstructured optical fibers capable of supporting PQSs. In 2019, Tam *et al.* [39] developed a numerical study that allowed the characterization of the stationary and dynamical properties of PQSs, also finding an approximate relation between the pulse energy and width, given by

$$E \approx 2.87\frac{|\beta_4|}{\gamma w_0^3}, \tag{1.2}$$

where β_4 is the 4OD coefficient and γ is the nonlinear parameter, while the relation for conventional solitons is

$$E = 4\text{arccosh}(\sqrt{2})\frac{|\beta_2|}{\gamma w_0}. \tag{1.3}$$

This analysis was generalized in the following year [40] to include significant 2OD terms. The authors found parameter regions where solutions with either exponentially decaying or oscillating tails exist, as well as evidence that the combination of these two orders of dispersion could improve soliton laser performance.

The previously mentioned works are all focused on conservative quartic solitons, but works on dissipative quartic solitons were developed in the meantime. The effects of high-order dispersion in Kerr frequency comb generation were first studied in 2017 by Bao *et al.* [41], showing the formation of stable quartic solitons with Gaussian shape, which were further explored in 2019 by Taheri and Matsko [42] in a comprehensive numerical analysis on dissipative PQSs in optical Kerr cavities. In 2020, Runge *et al.* [43] experimentally demonstrated the first mode-locked laser that emits PQSs, using a laser cavity dominated by negative 4OD. In 2022, Zhang *et al.* [44] found pulsating PQSs in the numerical simulation of a mode-locked fiber laser.

Contrary to the case of conservative quartic solitons, which only exist for negative 4OD, dissipative quartic solitons have been shown to exist for positive 4OD as well. In 2020, Runge *et al.* [45] theoretically and numerically demonstrated that a fiber laser with a cavity dominated by positive 4OD emitted self-similar pulses, and in 2022, Qian *et al.* [46] modeled a mode-locked fiber laser which generated dissipative solitons through the balance of positive 4OD, the Kerr nonlinearity, gain and loss.

When it comes to ultrashort laser applications, the $E \propto w_0^{-3}$ scaling [37, 39, 43] has attracted attention since, when compared to the energy-width scaling of conventional solitons ($E \propto w_0^{-1}$), quartic soliton lasers can generate ultrashort pulses with higher energies, which is an attractive feature for many applications [21]. However, this energy-width scaling has mostly been studied using conservative models [37, 39] with studies using dissipative models for mode-locked lasers showing contradictory results. While Runge *et al.* [43] found the aforementioned $E \propto w_0^{-3}$ relation for the case of negative 4OD by varying the laser pump power, Qian *et al.* [46] reported a relation of $E \propto w_0^3$ using positive 4OD and varying the gain saturation energy. These two different energy-width scalings for quartic solitons are plotted and compared with the conventional soliton scaling in Fig. 1.1. It remains unclear if this difference comes from the different dispersion regimes, or from a different energy-width dependence with the laser parameter that was varied, with the latter argument already being referred in [46].

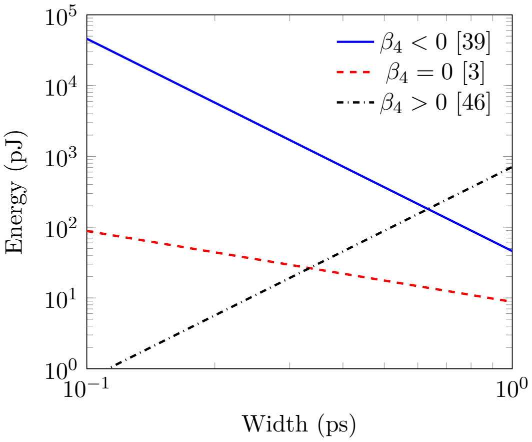

Figure 1.1: Energy-width scaling of PQSs following [39] with $\beta_4 = -0.08$ ps^{4}m^{-1} and $\gamma = 0.005$ W^{-1}m^{-1} (blue line), conventional solitons [3] with $\beta_2 = -0.024$ ps^{2}m^{-1} and the same γ (red dashed line) and of quartic solitons with positive 4OD, approximated from the results in [46].

Therefore, it is necessary to develop further work on the dissipative quartic soliton laser, to understand how the energy-width dependence is influenced by laser parameters and by the dispersion regime. Moreover, and regardless of the universal validity, or lack thereof, of the $E \propto w_0^{-3}$ relation in dissipative quartic solitons, there is potential interest in knowing how the energy of ultrashort pulses governed by 4OD can be maximized, for applications that require such short pulses with high energies [21]. The cubic quintic complex Ginzburg-Landau equation (CGLE) has been extensively studied in connection with mode-locked lasers [5, 47–49], but, despite having a relatively small number of parameters and allowing for semi-analytical approaches, it is not always possible to establish a valid relation between the CGLE and experimental parameters [50]. In [43, 46], a lumped model for the laser was used, which is an approach where each individual laser component is modeled by its own equation. Despite its high accuracy and the fact that it uses real experimental parameters, computations can become cumbersome. In between these two approaches, there is a distributed model, proposed in 2010 by Zaviyalov *et al.* [50] (in the absence of 4OD) which, through averaging procedures, can reduce the lumped model into a single evolution equation which contains the full saturable absorber term, unlike the CGLE. It was shown [50] that the results of the distributed model can be good approximations to the lumped model, thus being of potential interest in the numerical study of quartic solitons in mode-locked lasers.

1.2 Objectives and Outline

The main goals of this dissertation are to expand the distributed model presented in [50] to include 4OD (following our recent work [51]) in order to numerically simulate the generation of quartic dissipative solitons in mode-locked lasers, to study the energy-width behaviour in these lasers and to find ways to maximize the energy of ultrashort pulses. To that end, a plethora of laser parameters were varied considering both positive and negative 4OD, stationary pulse solutions were characterized, and the influence of the parameters on the pulse energy and width was analysed.

This dissertation is split into 5 chapters, with the current one providing an introduction, presenting a brief historical overview on the study of conventional, quartic, conservative and dissipative solitons in the field of optics, especially in the context of mode-locked lasers.

Chapter 2 addresses some key theoretical concepts related to dispersion, nonlinear optics, soliton formation and propagation, nonlinear pulse propagation equations in conservative and dissipative media as well as some background on passively mode-locked lasers and respective mathematical models. The distributed model used to simulate the laser is presented here.

Chapter 3 presents a dimensionless version of the distributed model, contains the considered laser parameters and describes the methods employed in the solving and characterization of solutions of the evolution equation.

Chapter 4 contains results from the numerical simulation of the mode-locked laser, shows and characterizes quartic soliton solutions for different signs of 4OD and in different laser parameter regions, and discusses the energy-width trends and ways to maximize the energy.

Chapter 5 summarizes the main results from the work, containing also the main conclusions and providing a brief outlook into future work.

1.3 Contributions

- D. Malheiro, M. Facão, M. I. Carvalho, Quartic solitons of a mode-locked laser distributed model, Optics Letters 48, 5639-5642 (2023), DOI: `10.1364/OL.504202`;

- D. Malheiro, M. Facão, M. I. Carvalho, Dissipative quartic solitons of a mode-locked laser distributed model, poster presentation at Extreme Waves International Workshop, Dresden, Germany, August 2023;

- M. Facão, D. Malheiro, M. I. Carvalho, Quartic dissipative solitons, presentation at Extreme Waves International Workshop, Dresden, Germany, August 2023.

2. Conservative and Dissipative Solitons

This chapter focuses on the main theoretical background for optical pulse propagation through conservative and dissipative nonlinear media. Section 2.1 introduces the concepts of dispersion and nonlinear effects in optical waveguides. In Section 2.2, the nonlinear Schrödinger equation (NLSE), a nonlinear propagation equation is presented and its conservative soliton solutions are introduced. Dissipative solitons, in particular in the framework of mode-locked fiber lasers, are addressed in Section 2.3, and models to describe them are discussed.

2.1 Dispersion and Nonlinear Effects

When light propagates through dielectric waveguides (e.g. optical fibers), it is subject to linear effects, namely loss and dispersion, as well as nonlinear effects such as the Kerr effect. The latter two are particularly important in the field of optical solitons, since its from their interplay that those waves are formed [3, 13].

2.1.1 Dispersion

Dispersion is the phenomenon that describes the frequency (ω) dependence of the refractive index (n) of a medium, i.e., $n \equiv n(\omega)$. In bulk media, the dispersion is originated by the interaction of the propagating electromagnetic wave with the internal charge structure of the medium, which will exhibit a response dependent on the frequency of the incident field. Therefore, its susceptibility, $\chi \equiv \chi(\omega)$, electric permittivity and refractive index, will all be frequency dependent. Consequently, the speed of light propagating in the medium, $c/n(\omega)$, where c is the speed of light in vacuum, will also depend on the frequency and thus, different spectral components of an incident optical pulse will travel at different speeds. In fact, the pulse travels with a group velocity, v_g, but each frequency experiences a different time delay and the pulse broadens in time. This phenomenon is known as group velocity dispersion (GVD) and is schematically represented in Fig. 2.1 [3, 52, 53].

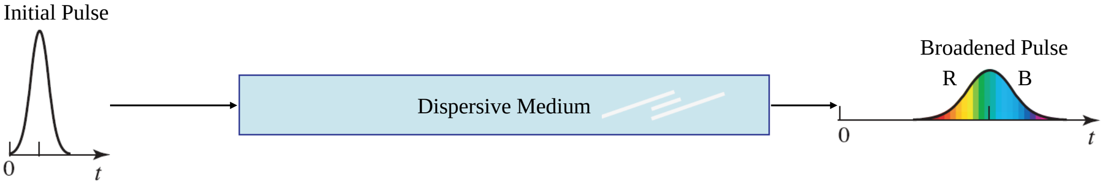

Figure 2.1: An optical pulse propagating through a dispersive medium, being broadened as result of the frequency dependence of the group velocity. In the depicted case, the low (red, denoted "R") frequency components travel faster than the high (blue, denoted "B") frequency component. Adapted from [53]

In the most basic terms, optical waveguides are made up of a core with reffractive index, n_{core}, surrounded by a cladding with an inferior reffractive index, n_{clad}. When light propagates in guided modes, it will experience an effective refractive index, n_{eff}, such that

$n_{\mathrm{clad}} \leq n_{\mathrm{eff}} \leq n_{\mathrm{core}}$. The effective reffractive index is defined by a propagation constant, β, with $\beta \equiv \beta(\omega) = \omega n_{\mathrm{eff}}/c$. The dispersion effects of each mode can be studied by expanding its corresponding β in a Taylor series about a central frequency ω_0:

$$\beta(\omega) = n(\omega)\frac{\omega}{c} = \beta_0 + \beta_1 (\omega - \omega_0) + \frac{\beta_2}{2!}(\omega - \omega_0)^2 + \frac{\beta_3}{3!}(\omega - \omega_0)^3 + \frac{\beta_4}{4!}(\omega - \omega_0)^4 + ... \quad (2.1)$$

where the dispersion orders, β_m are given by,

$$\beta_m = \left(\frac{d^m \beta}{d\omega^m}\right)_{\omega=\omega_0} \qquad (m = 0, 1, 2, ...). \quad (2.2)$$

The first order dispersion, β_1, is the inverse group velocity ($\beta_1 = 1/v_g$), and in works where higher orders ($m > 2$) of dispersion are absent, β_2 is commonly referred to as the GVD parameter. In this context, depending on the sign of β_2, two dispersion regimes can be defined. When $\beta_2 > 0$, low-frequency (red-shifted) components of an optical pulse travel at higher speed than the high-frequency components (blue-shifted). This is know as normal dispersion. When $\beta_2 < 0$, the opposite is true, and this is known as the anomalous dispersion regime [3, 4].

When higher orders of dispersion are considered, it becomes innacurate to refer to β_2 as the GVD parameter, since all β_m are, in fact, GVD parameters. Therefore, in the remainder of the work β_2 will be referred to as the second order dispersion (2OD) parameter. Even though higher orders of dispersion are often considered negligible, they become quite important in subpicosecond pulses [28, 40] and close to the frequency where β_2 is zero [3]. If a pulse propagates through a dispersive medium with pure dispersion β_m at a frequency ω_0, the inverse group velocity for frequencies at the vicinity of ω_0 is given by

$$\frac{1}{v_g} = \frac{1}{v_{g_0}} + \frac{1}{(m-1)!}\beta_m (\omega - \omega_0)^{m-1}, \quad (2.3)$$

where v_{g_0} is the the group velocity at ω_0 [54]. The effects of different orders of dispersion, be them negative or positive, can be evaluated by solving Eq. (2.3). Fig. 2.2 plots the inverse group velocity against the frequency shift under the effects of dispersion orders ranging from $m = 2$ to $m = 6$. Fig. 2.2(a) shows that the effect for all high even-orders of dispersion, is qualitatively the same as the $m = 2$ case. Therefore, in the case of negative β_m, with even m, the group velocity will monotonically increase with the frequency, with the opposite being true for $\beta_m > 0$. In contrast, the effect of odd orders of dispersion (Fig. 2.2(b)) leads to a non-monotonous dependence with the frequency and, for example, in the presence of β_3, low and high frequency components of the pulse travel more slowly ($\beta_3 > 0$) or more rapidly ($\beta_3 < 0$) than intermediate frequencies. This non-monotonic dependence of v_g with the frequency leads to pulse distortion, such that it becomes asymmetric with oscillations near the trailing or leading edge of the pulse, for positive and negative third order dispersion (3OD) respectively [3]. A qualitatively similar effect occurs for $m = 5$.

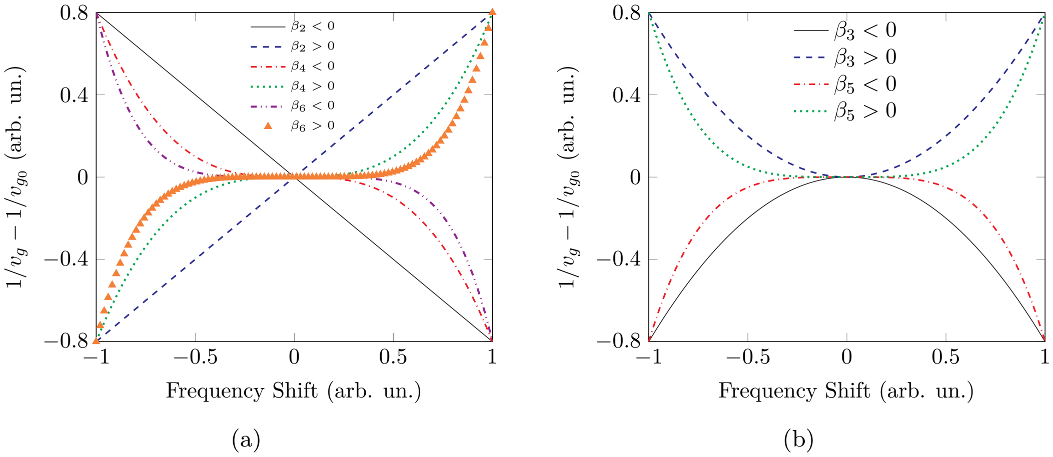

Figure 2.2: Frequency dependence of the inverse group velocity for pulses traveling in dispersive media with pure (a) even-order or (b) odd-order dispersion.

2.1.2 Nonlinearity

When an electromagnetic field interacts with a dielectric medium, a separation of bound charges occurs, resulting in induced electric dipole moments, which oscillate with the field [55]. In linear dielectric media, the polarization **P**, induced by the electric dipoles, is directly proportional to the electric field, **E**,

$$\mathbf{P} = \varepsilon_0 \chi^{(1)} \mathbf{E}, \tag{2.4}$$

where ε_0 is the vacuum permittivity and $\chi^{(1)}$ is the linear susceptibility, with its effects manifesting through the medium refractive index and attenuation [3, 53].

In nonlinear dielectric media, the interaction with the incident electromagnetic field leads to the anharmonic motion of the bound charges, giving rise to a wide range of nonlinear optical phenomena [3]. Furthermore, even media with small nonlinearities, such as silica-based optical fibers, can show a nonlinear response when interacting with intense electromagnetic fields (e.g. laser light) [56]. In these cases, polarization response to the incident **E** is described by the general relation

$$\mathbf{P} = \varepsilon_0 \left(\chi^{(1)} \cdot \mathbf{E} + \chi^{(2)} : \mathbf{EE} + \chi^{(3)} \vdots \mathbf{EEE} + \cdots \right), \tag{2.5}$$

where $\chi^{(j)}$ $(j = 1, 2, \ldots)$ is the j-th order susceptibility, with $\chi^{(j)}$ being a tensor of rank $j + 1$, and the vertical dots denoting the tensor product. The second order susceptibility, $\chi^{(2)}$, is only nonzero for media without an inversion symmetry at a molecular level, vanishing for silica fibers. Thus, the lowest order nonlinear effects originated in optical fibers are due to the third order susceptibility, $\chi^{(3)}$, responsible for the optical Kerr effect [3]. When a strong electric field interacts with the medium, electron orbits are deformed, and thus, the effective refractive index becomes dependent on the field intensity [56], being then given by

$$n_{\mathrm{eff}}(\omega, |E|^2) = \frac{c\beta}{\omega} = n_0(\omega) + n_2|E|^2, \tag{2.6}$$

where n_0 denotes the linear part of the refractive index, $|E|^2$ corresponds to the optical intensity and n_2 is the Kerr coefficient, which is directly related ot the third order susceptibility,

$$n_2 = \frac{3}{8n}\,\mathrm{Re}\left(\chi^{(3)}_{xxxx}\right). \tag{2.7}$$

Here, Re denotes the real part and the optical field was assumed to be linearly polarized along x, and so $\chi^{(3)}_{xxxx}$ is the only component contributing to the refractive index [3].

Recalling that $\beta = n_{\mathrm{eff}}\omega/c$, the intensity dependence of the refractive index in turn leads to an intensity dependence of the propagation constant. As a consequence, over the length of the waveguide, L, the pulse experiences a self-induced phase-shift, ϕ, during its propagation. This phenomenon is known as self-phase modulation (SPM) and the phase-shift is given by

$$\phi = \beta L = \left(n_0 + n_2|E|^2\right)\frac{2\pi}{\lambda_0}L, \tag{2.8}$$

where λ_0 is the wavelength. Since the intensity of the optical field is time (t) dependent, Eq. (2.8) implies that the phase shift is also time dependent and thus, the instantaneous optical frequency will differ across the pulse from its central value. The SPM induced frequency-shift, $\delta\omega$ is then given by

$$\delta\omega(t) = -\frac{\partial\phi}{\partial t} \propto -\frac{\partial|E|^2}{\partial t}. \tag{2.9}$$

This time dependent frequency shift is known as frequency chirping. When $\partial|E|^2/\partial t > 0$, i.e., at the leading edge of the pulse, $\delta\omega < 0$ and therefore, the frequency decreases (red-shift), whereas in the trailing edge ($\partial|E|^2/\partial t < 0$), the frequency increases (blue-shift). In other words, during propagation, new frequency components will be generated leading to an SPM-induced spectral broadening [3, 56].

SPM is only one of the plethora of nonlinear effects that exist. Others include cross-phase modulation and four-wave mixing, self-steepening and Raman scattering, among others [3], with the latter two having been studied in the framework of optical solitons [57]. Nonetheless the only conservative nonlinear effect considered in the remainder of the work is SPM.

2.2 The Nonlinear Schrödinger Equation

To study pulse propagation under the effects of GVD and SPM, the NLSE is often used. This equation is derived from the Maxwell equations under some simplifying assumptions and approximations. First, the medium is considered to be lossless (safeguarding energy conservation) and nonmagnetic; it is assumed that the nonlinear changes in the refractive index are small; the nonlinear response is considered instantaneous; the optical field is assumed to maintain its polarization along the propagation, to ensure the validity of a scalar approach; the optical field is considered to be quasi-monochromatic, which is valid for pulses as short as 0.1 ps. Finally, the slowly-varying pulse envelope approximation is considered, to separate the rapidly varying part of the electric field. Taking $W(z,t)$ as the slowly-varying pulse envelope, and only considering dispersion up to the second order for now (higher order generalizations will be discussed later), the NLSE can be written as [3, 58]

$$\frac{\partial W}{\partial z}+\beta_1\frac{\partial W}{\partial t}+i\frac{\beta_2}{2}\frac{\partial^2 W}{\partial t^2}=i\gamma|W|^2W. \tag{2.10}$$

Here z is the propagation coordinate and γ is the nonlinear parameter and is defined as

$$\gamma=\frac{n_2\omega_0}{cA_{\text{eff}}}, \tag{2.11}$$

where A_{eff} is the effective mode area, related to the spatial distribution of the electric field. The NLSE Eq. (2.10) can be further simplified by using a frame of reference moving at the group velocity. Thus, defining $t'=t-z/v_g=t-\beta_1 z$ as the retarded time, yields,

$$i\frac{\partial W}{\partial z}-\frac{\beta_2}{2}\frac{\partial^2 W}{\partial t'^2}+\gamma|W|^2W=0. \tag{2.12}$$

Depending on the initial pulse width, T_0, as well as the peak power, P_{peak}, either dispersive or nonlinear effects will dominate during pulse propagation. To better understand this, it becomes useful to introduce two length scales: the 2OD length, L_{2OD} and the nonlinear length, L_{NL}, which represent the lengths over which dispersive or nonlinear effects become important for pulse evolution. They are given by

$$L_{\text{2OD}}=\frac{T_0^2}{|\beta_2|},\quad L_{\text{NL}}=\frac{1}{\gamma P_{\text{peak}}}. \tag{2.13}$$

When the waveguide length is such that $L \ll L_{\text{NL}}$ and $L \ll L_{\text{2OD}}$, neither dispersive nor nonlinear effects manifest significantly during pulse propagation. When $L \ll L_{\text{NL}}$ and $L \sim L_{\text{2OD}}$, the pulse evolution is governed by GVD with nonlinear effects having little impact on pulse propagation. Likewise, if $L \ll L_{\text{2OD}}$, and $L \sim L_{\text{NL}}$, dispersive effects are negligible and pulse evolution is governed by SPM. However, when L is comparable to or greater than both L_{2OD} and L_{NL}, the pulse propagation is affected by an interplay of both dispersion and nonlinearity, which can lead to very interesting effects [3]. In the normal dispersion regime, the group velocity at the leading edge of the pulse, which has been red shifted due to SPM, increases, and the opposite occurs at the trailing edge, resulting in a much more rapid broadening than the one that would occur in the absence of SPM. In the anomalous dispersion regime, lower frequencies travel with lower values of v_g and vice-versa. Therefore, the group velocity will be lower in the leading edge of the pulse (red-shifted component) and higher in the trailing edge (blue-shifted component). Thus, these edges will tend toward the center of the pulse due to dispersion, leading to pulse compression. With a perfect balance of the effects of negative GVD and SPM, the pulse will propagate while maintaining its shape, i.e., an *optical soliton* is formed. Soliton formation through the interplay of GVD and SPM is illustrated in Fig. 2.3.

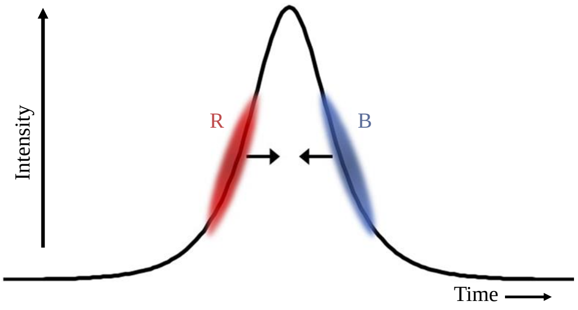

Figure 2.3: Schematic representation of soliton formation from the interplay of SPM and anomalous GVD. SPM induces a red-shift on the leading edge and a blue-shift on the trailing edge of the pulse, both of which tend to the center of the pulse through the action of negative even order dispersion. Adapted from [4].

Eq. (2.12) supports soliton solutions. To find them, stationary solutions of the form $W(z,t) = u(t)e^{i\sigma z}$ were considered, taking σ as a real propagation constant shift and u as a real valued function. Note that here, t is referring to the retarded time. The t' notation is henceforth dropped for the sake of simplicity. Introducing this ansatz in Eq. (2.12), and recalling that β_2 has to be negative for solitons to be formed, yields

$$-\sigma u + \frac{|\beta_2|}{2}\frac{d^2u}{dt^2} + \gamma u^3 = 0. \tag{2.14}$$

Eq. (2.14) supports the fundamental soliton solution, given by [4, 11]

$$u = \sqrt{\frac{2\sigma}{\gamma}}\,\mathrm{sech}\left(\sqrt{\frac{2\sigma}{|\beta_2|}}t\right), \tag{2.15}$$

with pulses thus taking the form of a hyperbolic secant curve. These solutions are referred to as *conventional solitons* from now on. Since u is real, conventional stationary solitons have a constant phase and are therefore unchirped, an effect that is directly related to the perfect balance of GVD and SPM. Under Eq. (2.15), the peak power and the width, w_0 of the fundamental soliton are

$$P_{\mathrm{peak}} = \frac{2\sigma}{\gamma}, \quad w_0 = \sqrt{\frac{2|\beta_2|}{2\sigma}}\mathrm{arccosh}(\sqrt{2}), \tag{2.16}$$

with the energy, E, following Eq. (1.3):

$$E = 4\mathrm{arccosh}(\sqrt{2})\frac{|\beta_2|}{\gamma w_0}. \tag{2.17}$$

Since σ can be chosen freely, Eq. (2.15) actually represents a family of soliton solutions with constant $\int u dt = \pi\sqrt{|\beta_2|/\gamma}$, with solutions for small σ being wider but having lower peak power than the narrow high peak power solutions for larger σ [4].

As previously mentioned, there are generalizations of the NLSE that include higher orders of dispersion [4],

$$i\frac{\partial W}{\partial z} + \sum_{m=2} i^m \frac{\beta_m}{m!}\frac{\partial^m W}{\partial t^m} + \gamma|W|^2 W = 0. \tag{2.18}$$

In soliton studies that include up to the fourth order, 3OD is usually undesirable, since it leads to soliton instability and radiation losses [59], although stationary soliton solutions in the presence of 2OD and fourth order dispersion (4OD) have been found when a weak 3OD term was present [30, 35]. The consequences of the presence of 3OD can be generalized to all odd-orders of dispersion, since they all have qualitatively the same effect on the group velocity (recall Eq. (2.3) and Fig. 2.2) and thus usually, in the context of solitons, only even orders of dispersion are considered. Truncating the expansion of β after the fourth order term and neglecting 3OD yields a generalized NLSE which includes both 2OD and 4OD terms,

$$i\frac{\partial W}{\partial z} - \frac{\beta_2}{2}\frac{\partial^2 W}{\partial t^2} + \frac{\beta_4}{24}\frac{\partial^4 W}{\partial t^4} + \gamma|W|^2 W = 0. \tag{2.19}$$

Eq. (2.19) supports soliton solutions (the discussion preceding Fig. 2.3 is also valid for even $m > 2$), known as *quartic solitons*, with a family of them being described by the Karlsson-Höök solution given by Eq. (1.1), valid when $\beta_2, \beta_4 < 0$ although quartic solitons with $\beta_2 > 0$, $\beta_4 < 0$ [37, 40] have also been found. In 2021, Runge *et al.* [54] reported an infinite hierarchy of solitons arising from pure negative high even orders of dispersion.

One important factor to take into consideration is that in the derivation of the NLSE, it was considered that the medium through which the light was propagating in was both lossless and gainless, ensuring energy conservation throughout the full propagation length. Therefore, the soliton solutions of the NLSE and its generalizations are commonly referred to as *conservative solitons*.

2.3 Dissipative Solitons in Mode-Locked Lasers

Although in conservative media solitons are formed from the balance between dispersion and nonlinearity, in the 1990s, it was found that solitons arise in nonlinear dispersive dissipative media, where a balance between nonlinear gain and loss is also present, thus opening the chapter of *dissipative solitons* [5, 60, 61]. Stationary dissipative solitons are originated when, alongside a balance between dispersion and nonlinearity, there is also a continuous energy exchange with the medium as well as a redistribution of the energy within the soliton itself. In effect, there are parts inside the pulse that generate energy and others which dissipate it [62]. This internal energy flow leads to a non-uniform phase profile and consequently to frequency chirping, unlike conservative solitons which are unchirped, due to having a constant phase profile [5]. Besides the more traditional stationary soliton behaviour, dissipative solitons can also exhibit pulsating, creeping and even exploding behaviours, all of which are only made possible due to the presence of the gain and loss mechanisms in the propagating medium [63, 64].

An interesting characteristic of dissipative solitons is that the equation parameters entirely define a fixed soliton solution, predetermining the profile, chirp and energy of the pulse, instead of defining a family of solutions as is the case with conservative solitons. In the latter case, the aforementioned quantities are determined by the initial conditions. This is a direct consequence of the perfect balance between gain and loss which is required for soliton formation. This stark contrast is illustrated in Fig. 2.4 [5].

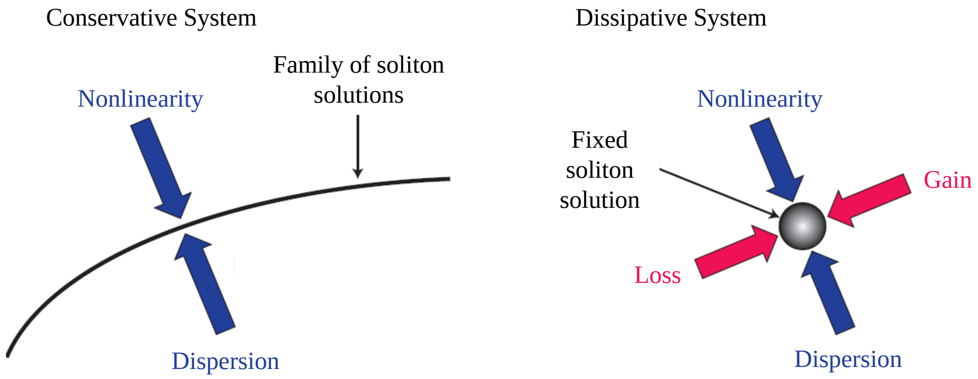

Figure 2.4: Qualitative differences of the impact of equation parameters on soliton solutions of conservative and dissipative systems. In the former case, dispersion and nonlinear parameters define a family of solution while in the latter, the introduction of gain and loss parameters yield a single solution. Adapted from [5].

Dissipative solitons are often studied in the framework of passively mode-locked fiber lasers [5]. Mode-locking is a technique used in the generation of ultrashort laser pulses which consists on locking the phases of the multiple laser modes to each other, forcing them to maintain the same relative phase. Consequently, the modes behave like Fourier components of a periodic function of time, leading to a periodic pulse train. This can be done by modulating the loss of the laser cavity at a frequency equal to the intermode frequency separations through either active or passive mode-locking methods. In active mode-locking, the loss modulation is done by employing either a shutter or an electro-optic or acousto-optic modulator, while in passive mode-locking, a saturable absorber (SA), a material whose absorption decreases as the intensity of light passing through it increases, is used instead [53, 65]. One type of SAs that is widely used is the semiconductor SA mirror, whose reflectivity increases with the intensity of the light. Suitable for wavelengths from 800 to 1600 nm, this type of SA allows the generation of pulses in the fs range, at powers that can go from a few mW to a few hundreds of W [53].

A class of lasers that has gained particular interest in the field of ultra-short pulse generation is the fiber laser [21], which offers several advantages over solid state lasers, such as higher optical powers, power-conversion efficiencies and beam quality (which persists to high-power operation), as well as superior resistance to temperature fluctuations and vibration. A particularly interesting feature of these lasers is the ability to operate on low-gain transitions, since the gain region can be arbitrarily long. In fiber lasers, rare-earth-doped fiber amplifiers are used as the gain medium, commonly using dopant ions such as erbium, neodymium, ytterbium and thulium. The energy pumping can be done using laser diode arrays or other fiber lasers [53].

This class of lasers can be mode-locked by the inclusion of a semiconductor SA mirror in the laser configuration. Silica-glass is the most common host material for the dopant ions, and its dispersion characteristics and nonlinearity which, combined with the gain mechanism of the amplifier and the losses at the SA, make mode-locked fiber lasers a very suitable environment for the generation and propagation of dissipative solitons. Multiple mode-locked fiber laser configurations exist [53, 66, 67], the simplest of which being made up of a pump diode laser, a doped fiber amplifier, an SA and an output coupler (OC), as illustrated in Fig. 2.5.

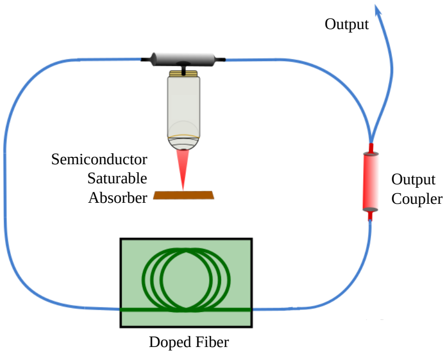

Figure 2.5: A simple mode-locked fiber laser scheme made up of a doped fiber amplifier, a semiconductor SA, and an OC. Not illustrated is the optical pumping required for laser operation, achieved through either a diode laser array or another fiber laser. Adapted from [68].

The study of dissipative soliton dynamics in mode-locked lasers was pioneered in the 1970s by Haus [47], who derived a master-equation which models the main physical effects occurring in these systems. This equation corresponds to the cubic complex Ginzburg-Landau equation (CGLE), but in the 1990s, Moores [69] reported that the inclusion of a quintic nonlinear term was fundamental for soliton stability in the presence of fast SAs. Thus, the cubic-quintic CGLE, which has been extensively used in the context of nonlinear optical systems, reads

$$i\frac{\partial q}{\partial Z} - \frac{D_2}{2}\frac{\partial^2 q}{\partial T^2} + |q|^2 q + \nu|q|^4 q = i\delta q + i\varepsilon|q|^2 + i\zeta\frac{\partial^2 q}{\partial T^2} + i\mu|q|^4 q. \tag{2.20}$$

where, T, Z, q are the normalized retarded time, propagation coordinate and pulse envelope respectively. The conservative terms of Eq. (2.20) are isolated on the left-hand side of the equation, with D_2 being the normalized 2OD parameter, and ν a parameter representing the saturation of the Kerr effect ($\nu < 0$). Likewise, the dissipative terms are isolated on the right side of Eq. (2.20) and here δ represents the linear loss ($\delta < 0$), ε the nonlinear gain ($\varepsilon > 0$), ζ the spectral filtering and μ the saturation of the nonlinear gain ($\mu < 0$). With the inclusion of these terms, Eq. (2.20), encapsulates, the fundamental physical effects required to build and operate a mode-locked laser, with the linear loss, nonlinear gain and its saturation accounting for the behaviour of the SA [5, 49].

Note that despite the fact that the form of the CGLE presented in Eq. (2.20) only includes 2OD, it can be generalized to include higher orders of dispersion, following the same logic that was used to generalize the NLSE in the previous Section. For example, a form of the CGLE that includes both 2OD and 4OD can be written as

$$i\frac{\partial q}{\partial Z} - \frac{D_2}{2}\frac{\partial^2 q}{\partial T^2} + \frac{D_4}{24}\frac{\partial^4 q}{\partial T^4} + |q|^2 q + \nu|q|^4 q = i\delta q + i\varepsilon|q|^2 + i\zeta\frac{\partial^2 q}{\partial T^2} + i\mu|q|^4 q, \tag{2.21}$$

where D_4 is the normalized 4OD parameter. The CGLE is in fact a distributed equation, because its terms are obtained through an averaging of light propagation effects in the system, in turn reducing the laser description into a single evolution equation. This approach allows for an analytical or semi-analytical treatment of the laser system and facilitates the search for stationary solutions and the analysis of their stability, as well as the discussion and understanding of physical effects in the system. Regardless, distributed equations allow for a generally good qualitative description of the laser system, and also good quantitative descriptions if the pulse does not suffer very significant alterations inside each cavity roundtrip. Despite its advantages and widespread use, even in the general context of distributed models, the CGLE does not take effects such as gain saturation and a non-instantaneous SA response into account. Moreover, a direct correspondence between the CGLE parameters as expressed in Eq. (2.20) with realistic laser parameters does not necessarily exist [5, 50].

Lumped models are a more accurate method to study the mode-locked fiber laser, by sequentially describing the propagation of light through each individual laser component, using at least one equation for each one of them. This approach not only allows for the consideration of the delayed effects the CGLE cannot account for, but also allows a direct correspondence with real experimental parameters, being however too involved to allow for analytical or semy-analytical analyses. Regardless, the lumped model is the starting point for all other average models [50]. In fact, the quintic term in the CGLE arises from approximations done in the reduction of the lumped model to a distributed one, with the actual saturation of the Kerr effect not being reached in most common laser setups [5, 70].

The lumped model is discussed extensively in [50], but in the simplest terms it can be reduced to three elements: a pulse propagation equation, an equation for the gain and finally an equation describing the SA response. Following the work of Runge *et al.* on the quartic soliton laser [43], the pulse propagation can be modeled by a modified NLSE which includes a gain term:

$$\frac{\partial W}{\partial z} + i\mathbf{D}\left(i\frac{\partial}{\partial t}\right)W = \frac{g}{2}W + i\gamma|W|^2 W. \tag{2.22}$$

The dispersion operator is defined as

$$\mathbf{D}\left(i\frac{\partial}{\partial t}\right) = \sum_{m=2}\frac{\beta_m}{m!}\left(i\frac{\partial}{\partial t}\right)^m, \tag{2.23}$$

and g is a saturated gain function such that

$$g = \frac{g_0}{1 + \int |W(z,t)|^2 dt / E_{\mathrm{sat}}}, \tag{2.24}$$

where g_0 is the small-signal gain, the integral represents the pulse energy and E_{sat} is the saturation energy. Finally, the SA is described by its transmittance, $\mathcal{T}$, modeled by a power transfer function,

$$\mathcal{T} = 1 - \frac{M}{1 + |W(z,t)|^2 / P_{\mathrm{sat}}}, \tag{2.25}$$

where M is the SA modulation depth and P_{sat} the saturation power, with $|W(z,t)|^2$ corresponding to the optical pulse power.

In 2010, Zaviyalov *et al.* [50] derived a distributed model that served as a bridge between the two aforementioned approaches. Since it is a distributed model, it has all the advantages of a model such as the CGLE, however, the authors developed it so that the SA term was not approximated. Moreover, and like the lumped model, its parameters are directly related to real experimental parameters. It is however, only valid under the assumption that the pulse is not very significantly altered during the propagation. Neglecting gain saturation effects, and assuming an instantaneous SA response, the description of the laser is given by

$$i\frac{\partial W}{\partial z} - \frac{1}{2}\left(\beta_2 + i g_0 T_2^2\right)\frac{\partial^2 W}{\partial t^2} = i\left(\frac{g_0 - k_{\mathrm{OC}}/L}{2}\right) W - \frac{i}{2}\frac{M/L}{1 + |W|^2/\bar{P}_{\mathrm{sat}}} - \bar{\gamma}|W|^2 W, \tag{2.26}$$

where T_2 is the inverse linewidth of the parabolic gain, k_{OC} is the OC loss and L is the cavity length. The parameters $\bar{P}_{\mathrm{sat}}$ and $\bar{\gamma}$ are the average parameters of the distributed model, associated with the SA saturation power, P_{sat}, and the nonlinear parameter, γ, respectively, and are given by:

$$\bar{P}_{\mathrm{sat}} = P_{\mathrm{sat}} \exp(-g_0 L), \quad \bar{\gamma} = \gamma \frac{\exp(g_0 L) - 1}{g_0 L}. \tag{2.27}$$

Much like the previously discussed models, the distributed model described by Eq. (2.26) can be expanded to include 4OD (following our recent work [51]), with the evolution equation thus taking the form:

$$i\frac{\partial W}{\partial z} - \frac{1}{2}\left(\beta_2 + i g_0 T_2^2\right)\frac{\partial^2 W}{\partial t^2} + \frac{\beta_4}{24}\frac{\partial^4 W}{\partial t^4} = i\left(\frac{g_0 - k_{\mathrm{OC}}/L}{2}\right) W - \frac{i}{2}\frac{M/L}{1 + |W|^2/\bar{P}_{\mathrm{sat}}} - \bar{\gamma}|W|^2 W. \tag{2.28}$$

3. Numerical Methods

The laser evolution equation as given by Eq. (2.28) does not support analytical solutions, therefore requiring the employment of numerical methods to solve it. These methods can either solve the partial differential equation (PDE) directly or they can take the indirect approach of first reducting the PDE into an ordinary differential equation (ODE) which can subsequently be numerically solved through the Newton conjugate-gradient (NCG), for example, as discussed in Section 3.1. For direct integration of the PDE, a pseudo-spectral method was used in Section 3.2. In Section 3.3 the stability of the solutions was studied numerically through a linear stability analysis.

Before implementing these methods, it is convenient to derive a dimensionless form of Eq. (2.28) in order to reduce the number of parameters. First, it is useful to recall Eq. (2.28)

$$i\frac{\partial W}{\partial z} - \frac{1}{2}\left(\beta_2 + ig_0T_2^2\right)\frac{\partial^2 W}{\partial t^2} + \frac{\beta_4}{24}\frac{\partial^4 W}{\partial t^4} = i\left(\frac{g_0 - k_{\mathrm{OC}}/L}{2}\right)W - \frac{i}{2}\frac{M/L}{1+|W|^2/\bar{P}_{\mathrm{sat}}} - \bar{\gamma}|W|^2W,$$

where z is the propagation coordinate, t the retarded time, W the slowly-varying pulse envelope, g_0 the small-signal gain, T_2 the inverse linewidth of the parabolic gain, P_{sat} the saturable absorber (SA) saturation power, β_2 and β_4 the second order dispersion (2OD) and fourth order dispersion (4OD) parameters respectively, k_{OC} the loss at the output coupler (OC), M the SA modulation depth and L the laser cavity length. Also recall that $\bar{P}_{\mathrm{sat}}$ and $\bar{\gamma}$ are the effective saturation power and nonlinear parameter respectively, given by Eq. (2.27). Following the change of variables

$$q = \left(\frac{\bar{\gamma}}{a}\right)^{1/2} W, \quad Z = az, \quad T = \left(\frac{2a}{g_0T_2^2}\right)^{1/2} t, \tag{3.1}$$

where $a = -g_0/2 + k_{\mathrm{OC}}/2L + M/2L$, Eq. (2.28) thus becomes

$$i\frac{\partial q}{\partial Z} - \frac{D_2}{2}\frac{\partial^2 q}{\partial T^2} + \frac{D_4}{24}\frac{\partial^4 q}{\partial T^4} + |q|^2q = i\alpha q + i\frac{\partial^2 q}{\partial T^2} - i\frac{\alpha+1}{1+\tau|q|^2}q, \tag{3.2}$$

with the normalized parameters being given by

$$D_2 = \frac{2\beta_2}{g_0T_2^2}, \quad D_4 = \frac{4\beta_4 a}{g_0^2T_2^4}, \quad \alpha = \frac{1}{a}\left(\frac{g_0}{2} - \frac{k_{\mathrm{OC}}}{2L}\right), \quad \tau = \frac{a}{\bar{P}_{\mathrm{sat}}\bar{\gamma}}. \tag{3.3}$$

One final aspect to take into consideration is the choice of parameter values. Throughout the work, a varying range of g_0, T_2 and P_{sat} parameter values was considered to find how these different terms influenced the solutions, in terms of pulse profile, phase, chirp, spectral profile, energy and width. These parameters were chosen carefully to ensure the existence and stability of soliton solutions. Although different values of β_4 were also tested, in most of the work, $|\beta_4| = 0.080$ ps^{4}m^{-1} was considered, with only the sign of the parameter being allowed to change. To isolate the contribution of the effect of 4OD, β_2 was set to zero in most cases and, whenever $\beta_2 \neq 0$, this parameter was only allowed to take a relatively small value of $|\beta_2| = 0.024$ ps^{2}m^{-1}. The other laser parameters were kept constant in all of the work, with the corresponding values being shown in Table 3.1. For realism, parameter values were taken from previous works on mode-locked lasers [43, 50].

Table 3.1: Constant laser parameter values.

Parameter	**Value**	**Unit**
k_{OC}	$-\ln(0.3)$	–
L	1	m
M	0.3	–
γ	0.005	W^{-1}m^{-1}

3.1 Newton Conjugate Gradient Method

Eq. (3.2) supports stationary solutions of the form

$$q(Z,T) = U(T)e^{i\sigma z}, \tag{3.4}$$

where U is a complex function and σ is a real propagation constant shift. Introducing this ansatz into Eq. (3.2) yields

$$U_Z + i\sigma U = G \tag{3.5}$$

where

$$G = \left[i\frac{D_4}{24}\partial_T^4 + \left(1 - i\frac{D_2}{2}\right)\partial_T^2 + \alpha + i|U|^2 - \frac{\alpha+1}{1+\tau|U|^2}\right] U. \tag{3.6}$$

Note that Eq. (3.5) stands for the case where U is allowed to depend on the propagation coordinate, Z. Since only stationary solutions are being considered, U is solely dependent on time and therefore $U_Z = 0$.

Both U and G can be separated into their real and imaginary parts,

$$U = U_r + iU_i, \quad G = G_r + iG_i, \tag{3.7}$$

with the subscripts r and i denoting, respectively, the real and imaginary parts of U and G. Considering this separation, Eq. (3.2) can be converted into a system of coupled nonlinear ODEs. Even though methods such as the shooting method [71] exist to solve such systems, convergence using this approach was not achieved for Eq. (3.5). Therefore, to solve the equation, the NCG method, as proposed in the works of Yang [72, 73], was used. Both these works and the theoretical overview on conjugate-gradient (CG) methods by Shewchuk [74] provide great details on the mathematical background and implementation of these methods. Not all of them will be repeated here but a brief overview, based on [72–74], will be provided to contextualize the implementation of the method in this work.

At first, σ is unknown but, as demonstrated in [73], it can be calculated from the real and imaginary parts of U and G, following,

$$\sigma = \frac{\langle U_i, G_i \rangle - \langle U_r, G_r \rangle}{2\langle U_r, U_i \rangle}. \tag{3.8}$$

with the inner product of two arbitrary functions of T, f and g, being defined as

$$\langle f, g \rangle = \int fg dT. \tag{3.9}$$

Inserting Eq. (3.7) into Eq. (3.5), yields

$$\begin{bmatrix} 0 & -\sigma \\ \sigma & 0 \end{bmatrix} \begin{bmatrix} U_r \\ U_i \end{bmatrix} = \begin{bmatrix} G_r \\ G_i \end{bmatrix} \tag{3.10}$$

which can be rewritten as

$$\mathbf{L}_0(\mathbf{u}) \equiv \begin{bmatrix} -\sigma U_i - G_r \\ \sigma U_r - G_i \end{bmatrix} = 0 \tag{3.11}$$

where $\mathbf{L}_0(\mathbf{u})$ is a function representing the differential equation and $\mathbf{u} = \left[\begin{smallmatrix} U_r \\ U_i \end{smallmatrix}\right]$. Before proceeding, it is important to clarify the notation used in this work. Capitalized letters in bold (e.g. $\mathbf{A}$) will represent matrices and operators, lower case letters in bold (e.g. $\mathbf{u}$) will denote vectors with all other letters (e.g. f, α) referring to scalar quantities, either real or complex.

The goal is to solve $\mathbf{L}_0(\mathbf{u}) = 0$ by first applying a Newton method and then the CG iterations. Denoting $\mathbf{u}_n$ as the approximation of $\mathbf{u}$ at the n-th iteration, the next approximation will be

$$\mathbf{u}_{n+1} = \mathbf{u}_n + \Delta \mathbf{u}_n \tag{3.12}$$

where the increment, $\Delta \mathbf{u}_n$, can be calculated through the linear Newton-correction [73, 75]

$$\mathbf{L}_{1n} \Delta \mathbf{u}_n = -\mathbf{L}_0(\mathbf{u}_n) \tag{3.13}$$

and $\mathbf{L}_{1n}$ is the linearization operator of function $\mathbf{L}_0(\mathbf{u}_n)$ obtained from the Taylor expansion of such function to the first order evaluated at u_n:

$$\mathbf{L}_0\left(\mathbf{u}_n + \tilde{\mathbf{u}}_n\right) = \mathbf{L}_0(\mathbf{u})_n + \mathbf{L}_1 \tilde{\mathbf{u}}_n + O(\tilde{\mathbf{u}}_n^2), \quad \tilde{\mathbf{u}}_n \ll 1. \tag{3.14}$$

This linearization operator, $\mathbf{L}_1$, is the counterpart of the Jacobian in systems of nonlinear ODEs [73, 75], and can be defined analytically through,

$$\mathbf{L}_1 \mathbf{u} = \mathbf{P}\mathbf{u} - \frac{\left\langle \begin{bmatrix} U_r \\ -U_i \end{bmatrix}, \mathbf{P}\mathbf{u} \right\rangle}{2\langle U_r, U_i \rangle} \begin{bmatrix} -U_i \\ U_r \end{bmatrix}, \tag{3.15}$$

where

$$\mathbf{P} = \begin{bmatrix} 0 & -\sigma \\ \sigma & 0 \end{bmatrix} - \mathbf{G}_1, \tag{3.16}$$

and $\mathbf{G}_1$ is the linearization operator of the vector function $\mathbf{g} = \left[\begin{smallmatrix} G_r \\ G_i \end{smallmatrix}\right]$. The calculation of this linearization operator will follow shortly.

The CG method is one of the most widely used iterative methods for solving large systems of linear equations [72, 74]. This method takes the linear equation as a minimization problem of a quadratic form, i.e., an arbitrary scalar function, f, of the form

$$f(\mathbf{x}) = \frac{1}{2}\langle \mathbf{x}, \mathbf{A}\mathbf{x} \rangle - \langle \mathbf{b}, \mathbf{x} \rangle + c, \tag{3.17}$$

where $\mathbf{x}$, $\mathbf{b}$, $\mathbf{A}$ and c are all arbitrary.

It can be shown [74] that the solution of the linear system of equations defined by $\mathbf{A}\mathbf{x} = \mathbf{b}$ corresponds to a minimum of the quadratic form defined in Eq. (3.17), as long as $\mathbf{A}$ is square, self-adjoint and positive-definite, i.e., if for every nonzero vector $\mathbf{u}$, $\langle \mathbf{u}, \mathbf{A}\mathbf{u} \rangle > 0$.

The basic principle of the CG method is the same as conjugate-directions method. In this latter one, if in iteration n the minimum is searched for in direction $\mathbf{d}_n$, in the next iteration the solution will be searched after in the *conjugate direction*, $\mathbf{d}_{n+1}$, which is $\mathbf{A}$-orthogonal to $\mathbf{d}_n$, i.e., $\langle \mathbf{d}_n, \mathbf{A}\mathbf{d}_{n+1} \rangle = 0$. In the CG method specifically, the search directions, $\mathbf{d}_n$ are constructed by the conjugation of the gradients which correspond to the residuals, $\mathbf{r}_n = -\nabla f(\mathbf{x}_n)$, according to

$$\mathbf{d}_{n+1} = \mathbf{r}_{n+1} + \frac{\langle \mathbf{r}_{n+1}, \mathbf{r}_{n+1} \rangle}{\langle \mathbf{r}_n, \mathbf{r}_n \rangle} \mathbf{d}_n, \tag{3.18}$$

It is generally accepted that the use of a preconditioning matrix, which improves the condition number of the matrix, is advantageous in the improvement of the efficiency of the CG method. Thus, introducing a matrix $\mathbf{M}$ which is self-adjoint, positive-definite, and is easy to invert, the system $\mathbf{A}\mathbf{x} = \mathbf{b}$ can be indirectly solved by computing

$$\mathbf{M}^{-1}\mathbf{A}\mathbf{x} = \mathbf{M}^{-1}\mathbf{b}. \tag{3.19}$$

If the condition number of $\mathbf{M}^{-1}\mathbf{A}$ is much smaller that the condition number of $\mathbf{A}$ alone, the method will converge much faster for Eq. (3.19). The choice of the preconditioner $\mathbf{M}$ is therefore very important but there are multiple possibilities that can be taken depending on the problem.

Considering an initial guess $\mathbf{x}_0$, the method can be summarized by

$$\mathbf{r}_0 = \mathbf{b} - \mathbf{A}\mathbf{x}_0, \tag{3.20a}$$

$$\mathbf{d}_0 = \mathbf{M}^{-1}\mathbf{r}_0, \tag{3.20b}$$

$$\gamma_n = \frac{\langle \mathbf{r}_n, \mathbf{M}^{-1}\mathbf{r}_n \rangle}{\langle \mathbf{d}_n, \mathbf{A}\mathbf{d}_n \rangle}, \tag{3.20c}$$

$$\mathbf{x}_{n+1} = \mathbf{x}_n + \gamma_n \mathbf{d}_n, \tag{3.20d}$$

$$\mathbf{r}_{n+1} = \mathbf{r}_n - \gamma_n \mathbf{A}\mathbf{d}_n, \tag{3.20e}$$

$$\delta_{n+1} = \frac{\langle \mathbf{r}_{n+1}, \mathbf{M}^{-1}\mathbf{r}_{n+1} \rangle}{\langle \mathbf{r}_n, \mathbf{M}^{-1}\mathbf{r}_n \rangle}, \tag{3.20f}$$

$$\mathbf{d}_{n+1} = \mathbf{M}^{-1}\mathbf{r}_{n+1} + \delta_{n+1}\mathbf{d}_n. \tag{3.20g}$$

This is the general CG method as specified in [74], and it was applied to solve the Newton-correction equation defined by Eq. (3.13). To use the CG method here however, the operator $\mathbf{L}_1$ has to be self-adjoint. Therefore it needs to be multiplied by its adjoint, $\mathbf{L}_1^{\mathrm{A}}$, and thus, the Newton-correction equation takes the form,

$$\mathbf{L}_{1n}^{\mathrm{A}}\mathbf{L}_{1n}\Delta\mathbf{u}_n = -\mathbf{L}_{1n}^{\mathrm{A}}\mathbf{L}_0\left(\mathbf{u}_n\right), \tag{3.21}$$

with the adjoint operator being given by

$$\mathbf{L}_1^{\mathrm{A}}\mathbf{u} = \mathbf{P}^{\mathrm{A}}\mathbf{u} + \frac{\left\langle \mathbf{u}, \begin{bmatrix} -U_i \\ U_r \end{bmatrix} \right\rangle}{2\langle U_r, U_i \rangle}\mathbf{P}^{\mathrm{A}} \begin{bmatrix} U_r \\ -U_i \end{bmatrix}, \tag{3.22}$$

and

$$\mathbf{P}^{\mathrm{A}} = \begin{bmatrix} 0 & \sigma \\ -\sigma & 0 \end{bmatrix} - \mathbf{G}_1^{\mathrm{A}}. \tag{3.23}$$

Now, the linearization operator, $\mathbf{G}_1$ has to be defined. Splitting the real and imaginary parts of G,

$$G_r = -\frac{D_4}{24}\partial_T^4 U_i + \frac{D_2}{2}\partial_T^2 U_i + \partial_T^2 U_r + \alpha U_r - \left(U_r^2 + U_i^2\right)U_i - \frac{\alpha+1}{1+\tau\left(U_r^2+U_i^2\right)}U_r, \tag{3.24}$$

$$G_i = \frac{D_4}{24}\partial_T^4 U_r - \frac{D_2}{2}\partial_T^2 U_r + \partial_T^2 U_i + \alpha U_i + \left(U_r^2 + U_i^2\right)U_r - \frac{\alpha+1}{1+\tau\left(U_r^2+U_i^2\right)}U_i, \tag{3.25}$$

$\mathbf{G}_1$ can then be calculated according to

$$\mathbf{G}_1 = \begin{bmatrix} \dfrac{\partial G_r}{\partial U_r} & \dfrac{\partial G_r}{\partial U_i} \\ \dfrac{\partial G_i}{\partial U_r} & \dfrac{\partial G_i}{\partial U_i} \end{bmatrix} = \begin{bmatrix} \partial_T^2 + G_{11} & -\dfrac{D_4}{24}\partial_T^4 + \dfrac{D_2}{2}\partial_T^2 + G_{12} \\ \dfrac{D_4}{24}\partial_T^4 - \dfrac{D_2}{2}\partial_T^2 + G_{21} & \partial_T^2 + G_{22} \end{bmatrix} \tag{3.26}$$

where

$$G_{11} = \alpha - 2U_rU_i - (\alpha+1)\frac{\tau\left(U_r^2 - U_i^2\right) - 1}{\left[1+\tau\left(U_r^2+U_i^2\right)\right]^2} \tag{3.27a}$$

$$G_{12} = -U_r^2 - 3U_i^2 + \frac{2\tau U_i\left(\alpha+1\right)}{\left[1+\tau\left(U_r^2+U_i^2\right)\right]^2} \tag{3.27b}$$

$$G_{21} = 3U_r^2 + U_i^2 + \frac{2\tau U_r\left(\alpha+1\right)}{\left[1+\tau\left(U_r^2+U_i^2\right)\right]^2} \tag{3.27c}$$

$$G_{22} = \alpha + 2U_r U_i - (\alpha + 1)\,\frac{\tau\left(U_i^2 - U_r^2\right) - 1}{\left[1 + \tau\left(U_r^2 + U_i^2\right)\right]^2}. \tag{3.27d}$$

Note that $\mathbf{G}_1$ is such that $\mathbf{G}_1^{\mathrm{A}} = \mathbf{G}_1^{\mathrm{T}}$ [73], with the T superscript denoting the transpose. Now, with all operators defined, the next step before the CG iterations is to choose a preconditioning matrix, $\mathbf{M}$. Following [73], $\mathbf{M}$ was chosen so that only the higher-derivative terms of $\mathbf{u}$ in $\mathbf{L}_1^{\mathrm{A}}\mathbf{L}_1\mathbf{u}$ are retained. A positive constant, C is also added, to ensure that $\mathbf{M}$ is positive definite and thus,

$$\mathbf{M} = \left[C + \left|i\frac{D_2}{2} - 1\right|^2 \partial_T^4 + \left(\frac{D_4}{24}\right)^2 \partial_T^8\right]\mathbf{I}_2, \tag{3.28}$$

where $\mathbf{I}_2$ is a 2×2 identity matrix and once again following [73], $C = 8$.

Using Eq. (3.20), the CG method applied to Eq. (3.21) thus becomes

$$\Delta\mathbf{u}_0 = 0, \tag{3.29a}$$

$$\mathbf{r}_0 = -\mathbf{L}_1^{\mathrm{A}}\mathbf{L}_0\left(\mathbf{u}_0\right), \tag{3.29b}$$

$$\mathbf{d}_0 = \mathbf{M}^{-1}\mathbf{r}_0, \tag{3.29c}$$

$$\gamma_n = \frac{\left\langle \mathbf{r}_n, \mathbf{M}^{-1}\mathbf{r}_n \right\rangle}{\left\langle \mathbf{d}_n, \mathbf{L}_1\mathbf{d}_n \right\rangle}, \tag{3.29d}$$

$$\Delta\mathbf{u}_{n+1} = \Delta\mathbf{u}_n + \gamma_n\mathbf{d}_n, \tag{3.29e}$$

$$\mathbf{r}_{n+1} = \mathbf{r}_n - \gamma_n\mathbf{L}_1\mathbf{d}_1, \tag{3.29f}$$

$$\delta_{n+1} = \frac{\left\langle \mathbf{r}_{n+1}, \mathbf{M}^{-1}\mathbf{r}_{n+1} \right\rangle}{\left\langle \mathbf{r}_n, \mathbf{M}^{-1}\mathbf{r}_n \right\rangle}, \tag{3.29g}$$

$$\mathbf{d}_{n+1} = \mathbf{M}^{-1}\mathbf{r}_{n+1} + \delta_{n+1}\mathbf{d}_n. \tag{3.29h}$$

Here $n = 0, 1, 2, \dots$ is the index of CG iterations, and the subscripts n were dropped from the $\mathbf{L}_1$ operators to simplify the notation. During implementation of the method, all derivatives were evaluated in the Fourier space, using the discrete Fourier transform (FT), with a time grid going from -50 to 50 with 2048 points. This was done in Matlab with the `fft` routine. As inputs, hyperbolic secant pulses were considered initially, but in further iterations the method was implemented with soliton solutions from previous simulations. The CG iterations were stopped once the Newton-correction solution, $\Delta\mathbf{u}_n$, dropped below a threshold of 10^{-4}. The Newton iterations were stopped once the overall error, given by $\max\{|\mathbf{L}_0(\mathbf{u}_n)|\}$, was smaller than 10^{-4}. Note however that if the amplitude of the solutions becomes too high, it might be difficult to achieve this latter error threshold in efficient time. Therefore, in such cases, a relative error limit of 0.025 was considered to break the cycle, with the relative error being calculated as $\max\{|\mathbf{L}_0(\mathbf{u}_n)|\}/\max\{u_n\}$.

While this method has the advantage of very fast convergence, it has the drawback of returning no information on the stability and the propagation of the solutions and so, other methods are necessary to investigate that.

3.2 Pseudo-spectral Method

To study the Z propagation and to verify the stability of solutions of the type given by Eq. (3.4) obtained through the NCG method, they were perturbed and taken as inputs in the integration of Eq. (3.2) through a pseudo-spectral method [76], evolving in Z with a fourth-order Runge-Kutta (RK4) method.

To start, Eq. (3.2) was rearranged, by first multiplying all terms by $-i$ and then by isolating the nonlinear terms in the right-hand side of the equation, such that

$$\frac{\partial q}{\partial Z} + \left(i\frac{D_2}{2} - 1\right)\frac{\partial^2 q}{\partial T^2} - i\frac{D_4}{24}\frac{\partial^4 q}{\partial T^4} - \alpha q = V, \tag{3.30}$$

where $V = i|q|^2 q - [(\alpha+1)\,q]\,/\,(1+\tau|q|^2)$ encompasses all the nonlinear terms from Eq. (3.2). Applying the FT to both sides of the equation yields

$$\frac{\partial \tilde{q}}{\partial Z} + \kappa\tilde{q} = \tilde{V}, \tag{3.31}$$

where the tilde denotes the FT, $\kappa = \omega^2 - \alpha - i\omega^2 D_2/2 - i\omega^4 D_4/24$ and ω is the frequency. Eq. (3.31) can be rewritten as

$$\frac{\partial\left[\tilde{q}\exp(\kappa Z)\right]}{\partial Z} = \tilde{V}\exp(\kappa Z), \tag{3.32}$$

which is an ODE that can be solved with an RK4 method [77–79].

Let us consider an arbitrary function $y(x)$ such that $f(x,y) = dy/dx$. To numerically solve this generic ODE, it is necessary to discretise the function domain so that two consecutive steps, x_n and x_{n+1} are evenly separated by a step size of h. In methods based on the approximation of derivatives from Taylor series expansions, the value of the function after $n+1$ steps, y_{n+1}, is approximated by

$$y_{n+1} = y_n + hy'_n + \frac{h^2}{2}y''_n + \ldots. \tag{3.33}$$

Therefore, to achieve higher accuracy, it is often necessary to consider higher-order derivatives. Runge-Kutta methods however evaluate the function at intermediate points within a single step thus guaranteeing higher accuracies even though only the first order derivative is being considered. The RK4 method evaluates the function in 4 points within the interval and has a global truncation error of $O\left(h^4\right)$. The solution at step x_{n+1} is given by

$$y_{n+1} = y_n + \frac{1}{6}\left(r_1 + 2r_2 + 2r_3 + r_4\right)h, \tag{3.34}$$

where r_i are increment functions defined as

$$r_1 = f\left(x_n, y_n\right) \tag{3.35a}$$

$$r_2 = f\left(x_n + \frac{h}{2}, y_n + r_1\frac{h}{2}\right) \tag{3.35b}$$

$$r_3 = f\left(x_n + \frac{h}{2}, y_n + r_2\frac{h}{2}\right) \tag{3.35c}$$

$$r_4 = f\left(x_n + h, y_n + r_3 h\right) \tag{3.35d}$$

To apply this for the numerical integration of Eq. (3.32), the time domain was once again discretised from -50 to 50 using 2048 points and discrete FTs were calculated through the `fft` Matlab routine. The variable Z varied depending on the considered equation parameters, but was chosen so that the pulse was allowed to propagate until it was stationary. Depending on the magnitude of Z, steps (dZ) between 10^{-4} and 10^{-5} were used to evenly discretise the Z domain. It is important to note that it was found that the convergence of the method and the amplitude of solutions was dependent on the step. If the step is too large (for the equation here presented, typically $dZ > 5 \times 10^{-3}$) the temporal profiles are different for different Z steps, but tend to converge for smaller steps. These results are illustrated in Fig. 3.1, where the peak power versus dZ is plotted for one specific set of equation parameters. In the figure, it is possible to observe that the peak power is converging to a fixed value as dZ is decreased. However, in general, it was found that the convergence was achieved whenever $dZ < 10^{-4}$.

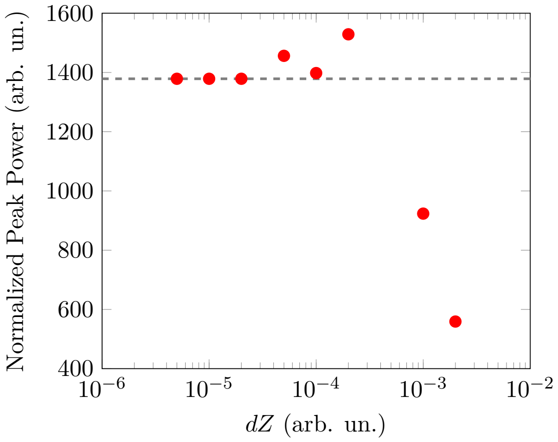

Figure 3.1: Dependence of the normalized peak power on dZ. As dZ decreases, the peak power tends to a constant value, marked by the black dashed line. Parameters: $\beta_2 = 0$, $\beta_4 = -0.080$ ps^{4}m^{-1}, $g_0 = 1.461$ m^{-1}, $P_{\text{sat}} = 83.3$ W, $T_2 = 100$ fs.

It was set that $y \equiv \tilde{q}\exp(\kappa Z)$, $x \equiv Z$ and $f(x, y) \equiv \tilde{V}\exp(\kappa Z)$. Note that $\tilde{V}$ is dependent on $\tilde{q}$ and therefore, it is necessary to evaluate its value in Z_n, $Z_n + dZ/2$ and $Z_n + dZ$, in each iteration of Eq. (3.35). Also note that the fact κ has a positive real part implies that as Z increases, $f(x, y)$ increases exponentially with it, greatly slowing down consecutive computations. This problem can be circumvented by exploiting the fact that Eq. (3.32) has translation symmetry in Z and, therefore, the equation can simply be solved in intervals of $[0, dZ]$. The $\tilde{q}\exp(\kappa Z)$ solution from each RK4 iteration can then be taken as the input for the next one using the same Z interval.

After the RK4 method has been completed, the exponential factor is divided to obtain $\tilde{q}$ and the inverse FT is applied to evaluate the dimensionless slowly-varying pulse envelope, q. Using the change of variables defined in Eq. (3.1) it is possible to convert the dimensionless results back to physical form.

3.3 Linear Stability Analysis

The numerical integration of Eq. (3.2) through the pseudo-spectral method using perturbed localized solutions as inputs can classify them as stable or unstable. However, since computation times can be rather long, it is not a very efficient approach to identify parameter regions where stable solutions exist. Thus, for that purpose, the eigenvalues of the linear stability operator for stationary solutions under Eq. (3.2) were calculated. This method can provide information on the stability of the solutions much more rapidly, since it does not require the integration of Eq. (3.2) in Z.

To obtain the linear stability operator, a small perturbation, be it $\eta \equiv \eta(Z,T)$, was added to stationary solutions given by Eq. (3.4), yielding

$$q(Z,T) = \left[U(T) + \eta(Z,T)\right] e^{i\sigma Z}. \tag{3.36}$$

Inserting Eq. (3.36) into Eq. (3.2), and considering only the first order terms in η, an evolution equation for the perturbation is obtained,

$$i\eta_Z + \mathbf{K}_{11}\eta + \mathbf{K}_{12}\eta^* = 0 \tag{3.37}$$

where the $*$ denotes the complex conjugate and the operators $\mathbf{K}_{11}$ and $\mathbf{K}_{12}$ are given by

$$\mathbf{K}_{11} = \frac{D_4}{24}\partial_T^4 - \left(\frac{D_2}{2} + i\right)\partial_T^2 - \sigma - i\alpha + 2|U|^2 + i\frac{1+\alpha}{\left(1+\tau|U|^2\right)^2} \tag{3.38}$$

$$\mathbf{K}_{12} = U^2 - i\frac{\left(1+\alpha\right)\tau U^2}{\left(1+\tau|U|^2\right)^2}. \tag{3.39}$$

Applying the complex conjugate to Eq. (3.37) yields

$$-i\eta_Z^* + \mathbf{K}_{11}^*\eta^* + \mathbf{K}_{12}^*\eta = 0. \tag{3.40}$$

Assuming that the evolution of the perturbation in Z is exponential, η and η^* can be defined as,

$$\eta(Z,T) = v(T)e^{i\lambda Z} + w^*(T)e^{-i\lambda^* Z}, \tag{3.41a}$$

$$\eta^*(Z,T) = v^*(T)e^{-i\lambda^* Z} + w(T)e^{i\lambda Z}. \tag{3.41b}$$

Substituting Eq. (3.41) into Eq. (3.37) and separating the terms dependent on $e^{i\lambda Z}$ and $e^{-i\lambda^* Z}$ leads to

$$-\lambda v + \mathbf{K}_{11}v + \mathbf{K}_{12}w = 0 \tag{3.42a}$$

$$\lambda^* w^* + \mathbf{K}_{11}w^* + \mathbf{K}_{12}v^* = 0 \tag{3.42b}$$

which, by rearranging the terms and applying the complex conjugate to Eq. (3.42b), can be written in the matrix form,

$$\mathbf{K}\begin{bmatrix} v \\ w \end{bmatrix} \equiv \begin{bmatrix} \mathbf{K}_{11} & \mathbf{K}_{12} \\ -\mathbf{K}_{12}^{*} & -\mathbf{K}_{11}^{*} \end{bmatrix}\begin{bmatrix} v \\ w \end{bmatrix} = \lambda \begin{bmatrix} v \\ w \end{bmatrix}. \tag{3.43}$$

The spectrum of operator $\mathbf{K}$ has both a continuous part and a discrete one, which consists of all the operator eigenvalues and will be the key to evaluate the stability of stationary solutions of Eq. (3.2). The parameter λ can be separated into its real and imaginary parts, i.e., $\lambda = \lambda_r + i\lambda_i$, and thus, η can be expressed as

$$\eta = ve^{i\lambda_r Z - \lambda_i Z} + w^{*}e^{-i\lambda_r Z - \lambda_i Z}. \tag{3.44}$$

It becomes apparent that the terms $e^{\pm i\lambda_r Z}$ lead to oscillations in Z, since these exponentials are complex. The $e^{-\lambda_i Z}$ exponentials are real, and very important to determine whether the perturbation will decay or destabilize the solution. If $\lambda_i > 0$, the perturbation decays exponentially with Z but if $\lambda_i < 0$, the perturbation will grow exponentially, rendering the solution unstable. Therefore, the solutions of Eq. (3.2) are unstable whenever the imaginary parts of eigenvalues of the linear stability operator, $\mathbf{K}$ is negative. Note that it can be shown that $\lambda = 0$ is always an eigenvalue present in the discrete spectrum.

The eigenvalues of $\mathbf{K}$ can be calculated numerically by approximating the second and fourth-order derivatives using central finite differences for v and w, namely [79]

$$\frac{d^2y_n}{dT^2} = \frac{y_{n-1} - 2y_n + y_{n+1}}{dT^2} + O(dT^2), \tag{3.45}$$

$$\frac{d^4y_n}{dT^4} = \frac{y_{n-2} - 4y_{n-1} + 6y_n - 4y_{n+1} + y_{n+2}}{dT^4} + O(dT^2), \tag{3.46}$$

where y_n is the $y(T)$ value at T_n, one generic point of the equally spaced mesh $T_n = T_0 + ndT$, with dT being the mesh element size and if N is the number of mesh elements, $n = 0, 1, ..., N$. Thus, using Eqs. (3.45) and (3.46), the matrix elements of $\mathbf{K}$ were calculated and its eigenvalues, λ, were computed through the Matlab function, `eig`. Then, the sign of the imaginary part of the eigenvalues was analyzed to determine whether the solution is stable or not.

To calculate the continuous spectrum, the limit of $\mathbf{K}$ when $T \to \pm\infty$, K_∞ is first considered. In this case, $U_{T\to\pm\infty} = 0$, and so

$$\mathbf{K}_\infty = \begin{bmatrix} \frac{D_4}{24}\partial_T^4 - \left(\frac{D_2}{2} + i\right)\partial_T^2 - \sigma + i & 0 \\ 0 & -\frac{D_4}{24}\partial_T^4 + \left(\frac{D_2}{2} - i\right)\partial_T^2 + \sigma - i. \end{bmatrix} \tag{3.47}$$

Then, assuming that v and w oscillate in time, i.e.,

$$v = v_0 e^{isT}, \quad w = w_0 e^{irT}, \tag{3.48}$$

where both s and r are real, and introducing Eq. (3.48) into $\mathbf{K}_\infty[\begin{smallmatrix} v \\ w \end{smallmatrix}] = \lambda[\begin{smallmatrix} v \\ w \end{smallmatrix}]$, leads to the system of equations

$$\begin{cases} \lambda_r = \dfrac{D_2}{2}\left(\lambda_i - 1\right) + \dfrac{D_4}{24}\left(\lambda_i - 1\right)^2 - \sigma, & \lambda_r < -\sigma \\ \lambda_r = -\dfrac{D_2}{2}\left(\lambda_i - 1\right) - \dfrac{D_4}{24}\left(\lambda_i - 1\right)^2 + \sigma, & \lambda_r > \sigma \end{cases} . \tag{3.49}$$

These equations describe two branches of half parabolas which, when $D_2 = 0$, have their axes at $\lambda_i = 1$ and vertices at $(-\sigma, 1)$ and $(\sigma, 1)$, for the first and second equations, respectively. An example of the linear stability operator spectrum for an unstable solution, highlighting both the continuous and discrete parts, is shown in Fig. 3.2(a). This spectrum was obtained for a solution with $g_0 = 1.50\ \mathrm{m}^{-1}$, $T_2 = 100$ fs, $P_{\mathrm{sat}} = 80$ W, $\beta_2 = 0$ and $\beta_4 = -0.080\ \mathrm{ps}^4\mathrm{m}^{-1}$. To confirm the instability of this solution, it was perturbed by increasing its amplitude by 1% and used as an input for the integration in Z through the pseudo-spectral method. The evolution of the peak power along Z is plotted in Fig. 3.2(b), showing that it increases abruptly at the very start of the propagation. Subsequently, instead of evolving to a constant value, the peak power oscillates uncontrolled.

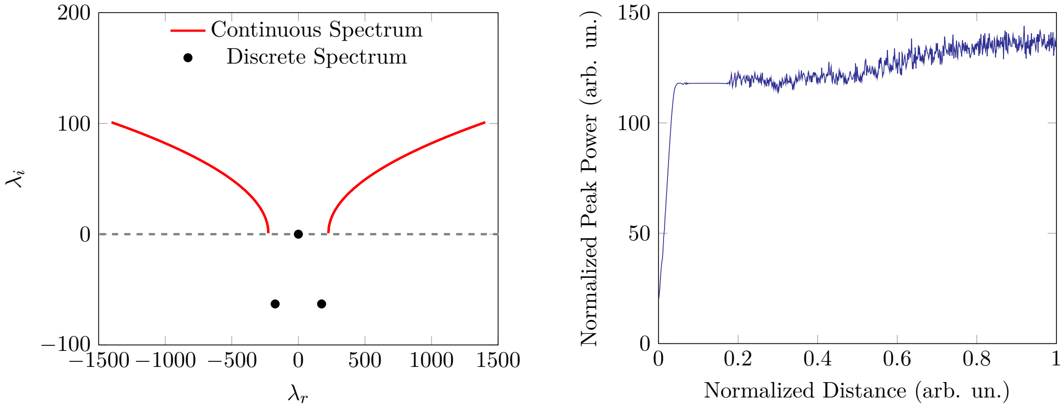

(a) (b)

Figure 3.2: (a) Linear stability operator spectrum of the solution of Eq. (3.2) obtained with $\beta_2 = 0$, $\beta_4 = -0.080\ \mathrm{ps}^4\mathrm{m}^{-1}$, $g_0 = 1.50\ \mathrm{m}^{-1}$, $T_2 = 100$ fs, $P_{\mathrm{sat}} = 80$ W. The eigenvalues with negative imaginary parts are evidence that this particular solution is unstable, as shown by the erratic oscillations in the peak power in (b).

4. Results and Discussion

In this chapter, the results from the numerical simulation of pulse propagation on a mode-locked laser with fourth order dispersion (4OD) using a distributed model are presented and discussed. Section 4.1 shows and describes the different kinds of pulse solutions, as well as the respective phase, chirp and spectra, discussing the main parameters that influence them. In Section 4.2, the energy and width dependence with each parameter is analyzed, and the energy-width scaling of dissipative quartic solitons is investigated. Section 4.3 concludes the chapter with a search for a parameter region which maximizes pulse energy.

4.1 Quartic Soliton Solutions of the Distributed Model

Using the methods specified in Chapter 3 and the parameters on Table 3.1, stationary quartic soliton solutions of the mode-locked laser distributed model (as per Eq. (2.28)) were found. These solutions were obtained by considering a varying range of small-signal gain, g_0, inverse linewidth of the parabolic gain, T_2 and saturation power, P_{sat}, values for both positive and negative 4OD either in the presence or in the absence of second order dispersion (2OD).

While the g_0 and P_{sat} parameters primarily impact the peak power of the pulse solutions, the value of T_2 and the sign of β_4 are the parameters that mainly influence the pulse shape. As an example, in Fig. 4.1, the quartic soliton amplitude profiles for $\beta_4 = \pm 0.08$ ps^{4}m^{-1} when $\beta_2 = -0.024$ ps^{2}m^{-1}, $g_0 = 1.45$ m^{-1}, $T_2 = 100$ fs and $P_{\text{sat}} = 80$ W are represented. For the sake of comparison with conventional solitons, the pulse profile for $\beta_4 = 0$ is also plotted, taking the approximate shape of a hyperbolic secant, as is typical in this type of solitons. For $\beta_4 < 0$, the pulses are Gaussian with symmetrically oscillating tails, which are particularly noticeable in logarithmic scale, whereas for $\beta_4 > 0$, the pulses come in the shape of a hyperbolic secant atop a broader pedestal of exponentially decaying tails.

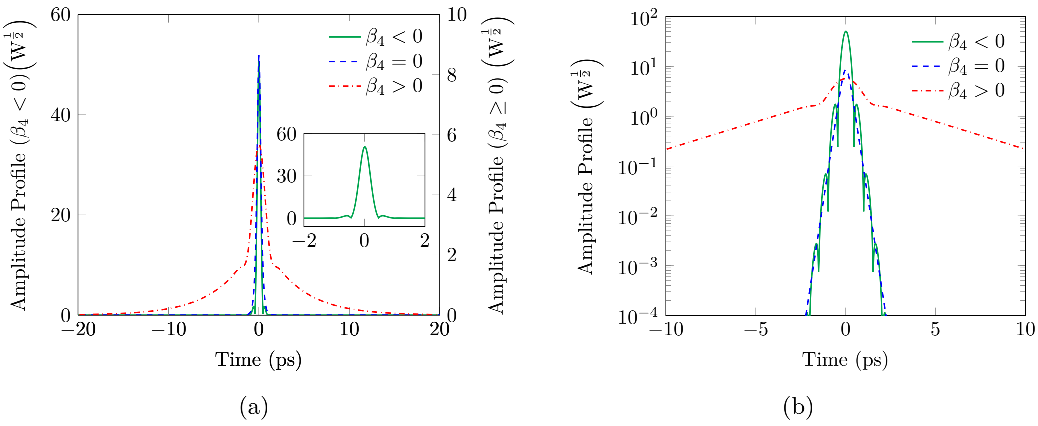

(a)

(b)

Figure 4.1: Pulse profiles in (a) linear and (b) logarithmic scale for $\beta_4 = \pm 0.080$ and 0 ps^{4}m^{-1}. Note that in (a), the left-hand side axis refers to the pulse with $\beta_4 < 0$ and the right-hand side axis refers to the remaining ones. The inset highlights the oscillations in the tails of the solution with $\beta_4 < 0$. Parameters: $\beta_2 = -0.024$ ps^{2}m^{-1}, $g_0 = 1.45$ m^{-1}, $T_2 = 100$ fs and $P_{\text{sat}} = 80$ W.

Even though this work is mainly focused on quartic solitons and therefore on the effects of 4OD, before moving on to other solution characteristics and the influence of other equation parameters, it is important to have an understanding on the effect of β_2 on the solutions of Eq. (2.28). Considering $\beta_4 = \pm 0.080$ ps^{4}m^{-1}, Eq. (2.28) was solved considering $\beta_2 = \pm 0.024$ ps^{2}m^{-1} and $\beta_2 = 0$, with the results being shown in Fig. 4.2. For both negative (Fig. 4.2(a)) and positive (Fig. 4.2(b)) 4OD, solutions exist for both signs of β_2, as well as when this dispersion parameter vanishes. When $\beta_4 < 0$, it is evident that the difference in sign of β_2 did not significantly impact the pulse shape, just slightly altering the peak power, which is highest for $\beta_2 < 0$ and lowest for $\beta_2 > 0$. The shape of the pulse profile in the $\beta_4 > 0$ regime is slightly different when $\beta_2 < 0$ than in the other two cases, with the pedestal being narrower in the former case, with only slight changes in the peak power distinguishing the latter cases. It is important to note however that while in the case of $\beta_4 < 0$, g_0, T_2 and P_{sat} parameters were found such that stable solutions exist for the three values of β_2, in the case of $\beta_4 > 0$, g_0 had to be changed for a stationary solution with $\beta_2 > 0$ to be found (solution stability will be discussed later). In spite of this, these results still prove that soliton solutions can be found for any sign of β_2 with both negative and positive 4OD, and also that the main contribution to the pulse shape comes from 4OD. Note however, that only a relatively small value of $|\beta_2|$ when compared to $|\beta_4|$ was tested, and if $|\beta_2|$ were to be increased, these conclusions may not hold true. Regardless, in the remainder of the work, whenever the effects of the dispersion themselves are not being discussed, β_2 will be set to zero.

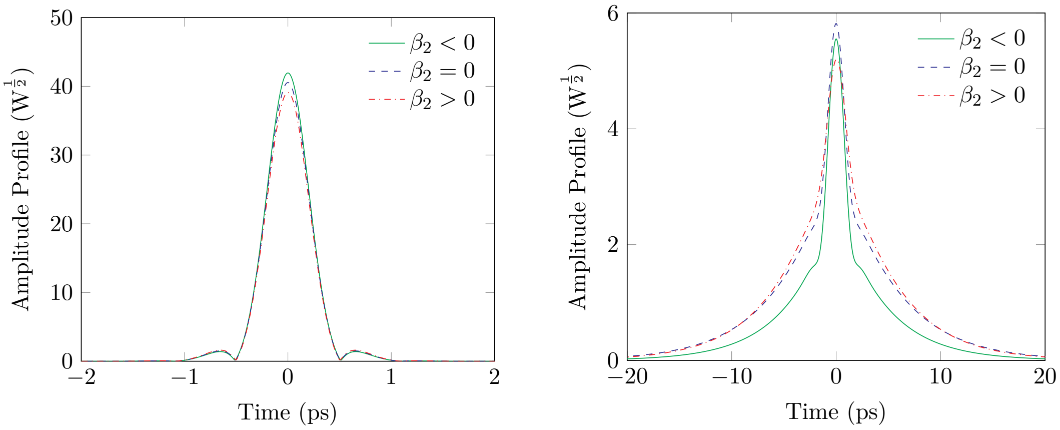

(a) (b)

Figure 4.2: Pulse profiles for negative, zero and positive β_2, for (a) $\beta_4 = -0.080$ ps^{4}m^{-1}, $g_0 = 1.40$ m^{-1}, $T_2 = 100$ fs and $P_{\text{sat}} = 80$ W; and (b) $\beta_4 = -0.080$ ps^{4}m^{-1}, $T_2 = 110$ fs, $P_{\text{sat}} = 80$ W and $g_0 = 1.45$ m^{-1} when $\beta_2 \leq 0$ and $g_0 = 1.46$ m^{-1} for $\beta_2 > 0$. In all non-vanishing cases, $|\beta_2| = 0.024$ ps^{2}m^{-1}.

Since the distributed model contains dissipative terms, all the pulse solutions showed a non-uniform phase profile, due to the existence of an intrapulse energy flow [62], which in turn led to frequency chirping. Both the phase and the chirp were found to be dependent on β_4, as shown in Fig. 4.3. The phase profile for $\beta_4 < 0$ (Fig. 4.3(a)) has a stair-like shape, with steps of approximately constant phase values separated by abrupt π jumps, caused by the oscillations in the pulse tails. These π jumps also occur in conservative quartic solitons, representing sign changes in the real envelope function. In this case however, the phase is always alternating between 0 to π, instead of forming the stair like structure seen in Fig. 4.3(a), since energy transfer mechanisms are absent [39, 80]. In the dissipative case, the π shifts result in chirp spikes (Fig. 4.3(d)), with the chirp itself being close to 0 in the approximately constant phase sections. The phase and the chirp follow similar behaviours for zero and positive 4OD, with phase profiles (Figs. 4.3(b) and 4.3(c) for $\beta_4 = 0$ and $\beta_4 > 0$ respectively) following an approximately triangular shape, as is typical in dissipative solitons. This leads to the chirp shown in Figs. 4.3(e) and 4.3(f) ($\beta_4 = 0$ and $\beta_4 > 0$ respectively), with the frequency chirp being constant and negative at the leading edge ($t < 0$) of the pulse, increasing approximately linearly across the pulse center (with a slight overshoot when $\beta_4 > 0$), until it becomes positive and constant at the trailing ($t > 0$) edge of the pulse.

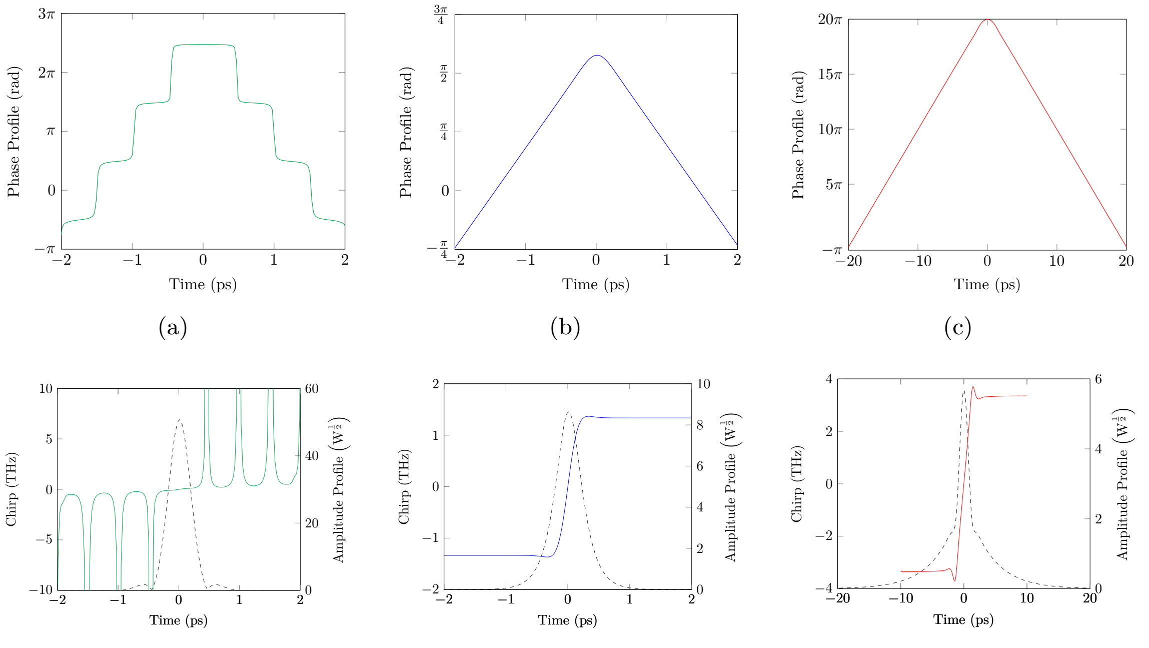

(a) (b) (c)

(d) (e) (f)

Figure 4.3: Phase profiles (top row) and chirp (bottom row) of soliton solutions with (a) and (d) $\beta_4 = -0.080$ ps^{4}m^{-1}; (b) and (e) $\beta_4 = 0$ and (c) and (f) $\beta_4 = 0.080$ ps^{4}m^{-1}. Parameters: $\beta_2 = -0.024$ ps^{2}m^{-1}, $g_0 = 1.45$ m^{-1}, $T_2 = 100$ fs and $P_{\text{sat}} = 80$ W.

The spectral shape (Fig. 4.4) is also greatly influenced by the sign of β_4. The spectral profiles for negative and zero 4OD are, in general, somewhat similar with both spectra decaying exponentially (evidenced in logarithmic scale in Fig. 4.4(b)), with the main difference being at the peak of the spectra, which is much flatter for $\beta_4 < 0$ because of the amplitude oscillations the pulse experiences [39]. The spectrum for positive 4OD is quite different from the other two however, instead having two peaks at the edges, occurring at symmetrical frequencies and with the same intensity. Much like when $\beta_4 \leq 0$, the spectrum for $\beta_4 > 0$ decays exponentially, but as is noticeable in Fig. 4.4(b), this decay is much steeper than in the previous cases.

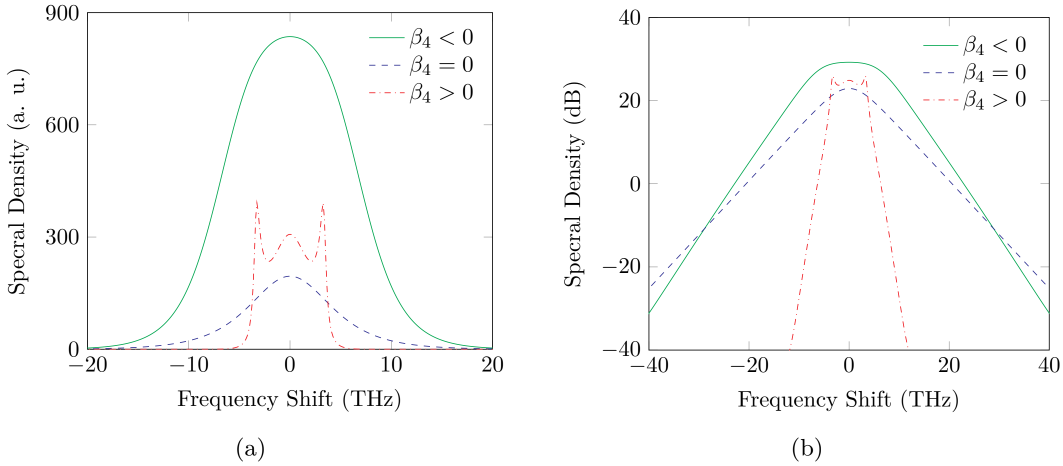

(a) (b)

Figure 4.4: Pulse spectra in (a) linear and (b) logarithmic scale for $\beta_4 = \pm 0.080$ and 0 $\mathrm{ps^4 m^{-1}}$. Parameters: $\beta_2 = -0.024$ $\mathrm{ps^2 m^{-1}}$, $g_0 = 1.45$ $\mathrm{m^{-1}}$, $T_2 = 100$ fs and $P_{\mathrm{sat}} = 80$ W.

The other parameter that influences the pulse shape is T_2, the inverse linewidth of the parabolic gain, which is a parameter that is directly related to the spectral filtering term in Eq. (2.28), i.e., $-\frac{i}{2} g_0 T_2^2 \partial^2 W / \partial t^2$. Fig. 4.5(a) shows the impact of increasing T_2 in the shape of pulses obtained with $\beta_4 = -0.080$ $\mathrm{ps^4 m^{-1}}$. For $T_2 = 100$ fs, the soliton profile takes the same shape as the one presented for $\beta_4 < 0$ in Fig. 4.1(a). However, as T_2 increases to 150 fs, and further so to 200 fs, the oscillations in the tails begin to flatten, until they are completely absent for $T_2 = 250$ fs. Moreover, for the latter T_2 value and greater ones the soliton profile is now hyperbolic secant shaped. The flattening of the oscillations and the transition in pulse shape is further evidenced in logarithmic scale in Fig. 4.5(b). A similar behaviour exists in the presence of positive 4OD. In Fig. 4.5(c), with $\beta_4 = 0.080$ $\mathrm{ps^4 m^{-1}}$ and $T_2 = 115$ fs, the pulse has a similar shape to the pulse for positive 4OD in Fig. 4.1(a), i.e., a hyperbolic secant sitting upon a pedestal with exponentially decaying tails. Changing T_2 to 200 fs, the pedestal contracts and the soliton profile becomes purely hyperbolic secant shaped. This is more noticeable in logarithmic scale (Fig. 4.5(d)), where, for $T_2 = 200$ fs, it can be seen that the base of the pulse is much narrower and the tails are clearly defined by straight lines converging near the peak, compared to the rapid broadening that occurs for $T_2 = 115$ fs.

With the pulse shape varying with T_2, it is expected that the phase and the chirp are also influenced by this parameter. In fact, for $\beta_4 < 0$, the phase profile (Fig. 4.6(a)) transitions from the stair-like shape that occurs for $T_2 = 100$ fs (blue solid curve) to a more triangular shape when $T_2 = 250$ fs (yellow dotted curve). As T_2 increases to 150 fs (red dashed line) and further so to 200 fs (green dash dotted line), the previously constant phase steps start to acquire a negative (trailing edge) or positive (leading edge) slope and the π jumps in the phase are also much less abrupt, having a finite slope. This evolution is translated in the chirp, with the sharp peaks occurring for $T_2 = 100$ fs, beginning to take the form of damped oscillations for T_2 values of 150 fs and 200 fs, until a chirp curve similar to the ones portrayed

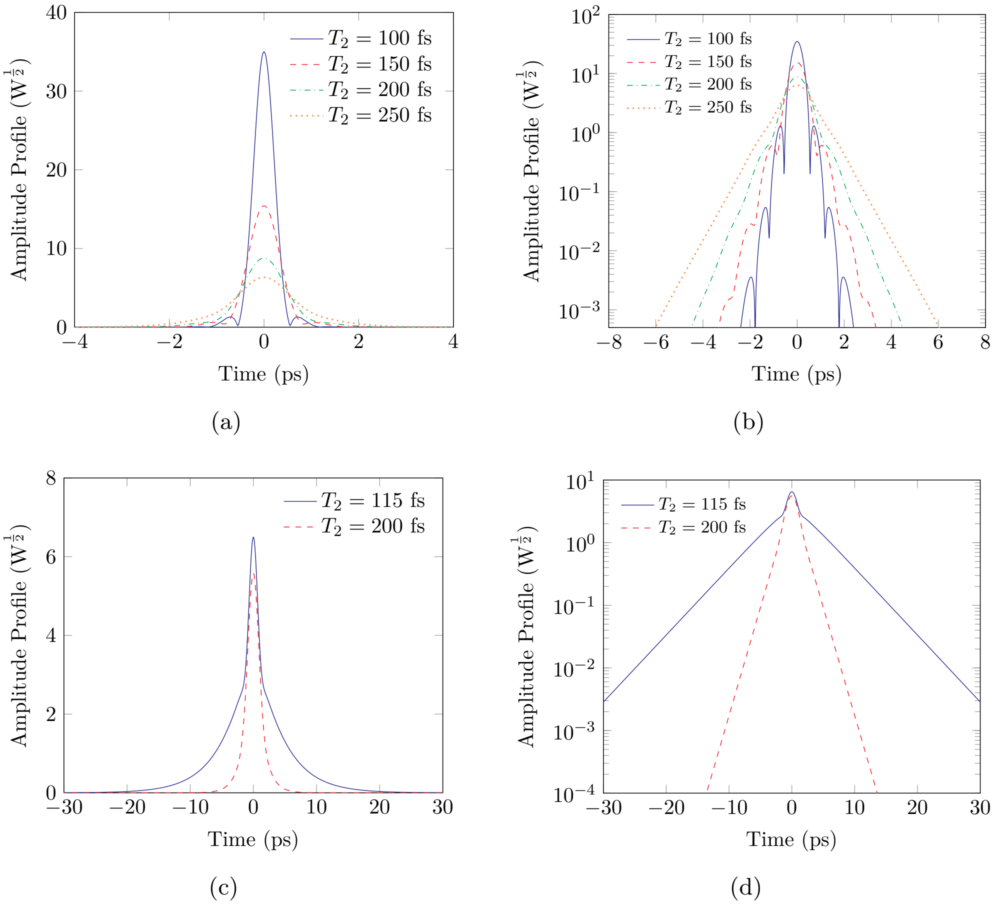

(a) (b)

(c) (d)

Figure 4.5: Pulse shapes for different values of T_2 for (a), (b) $\beta_4 = -0.080\ \mathrm{ps}^4\mathrm{m}^{-1}$, $P_{\mathrm{sat}} = 3$ W and $g_0 = 1.36\ \mathrm{m}^{-1}$, and (c), (d) $\beta_4 = 0.080\ \mathrm{ps}^4\mathrm{m}^{-1}$, $P_{\mathrm{sat}} = 80$ W and $g_0 = 1.48\ \mathrm{m}^{-1}$, in linear and logarithmic scale, respectively. In both cases, $\beta_2 = 0$.

in Figs. 4.3(e) and 4.3(f) ($\beta_4 \geq 0$) is obtained with $T_2 = 250$ fs. In fact, as was previously discussed, an increase in T_2 leads to a flattening of the oscillations, which in turn makes the phase jumps less steep and as the oscillations become flatter, the phase takes a linear profile at each pulse edge. In direct contrast, for $\beta_4 > 0$ (Figs. 4.6(c) and 4.6(d)), the differences in phase profile and chirp with T_2 are not particularly noticeable. In effect, the pulses obtained with positive 4OD do not have oscillations, which are the cause of the sharp π jumps in the phase when $\beta_4 < 0$.

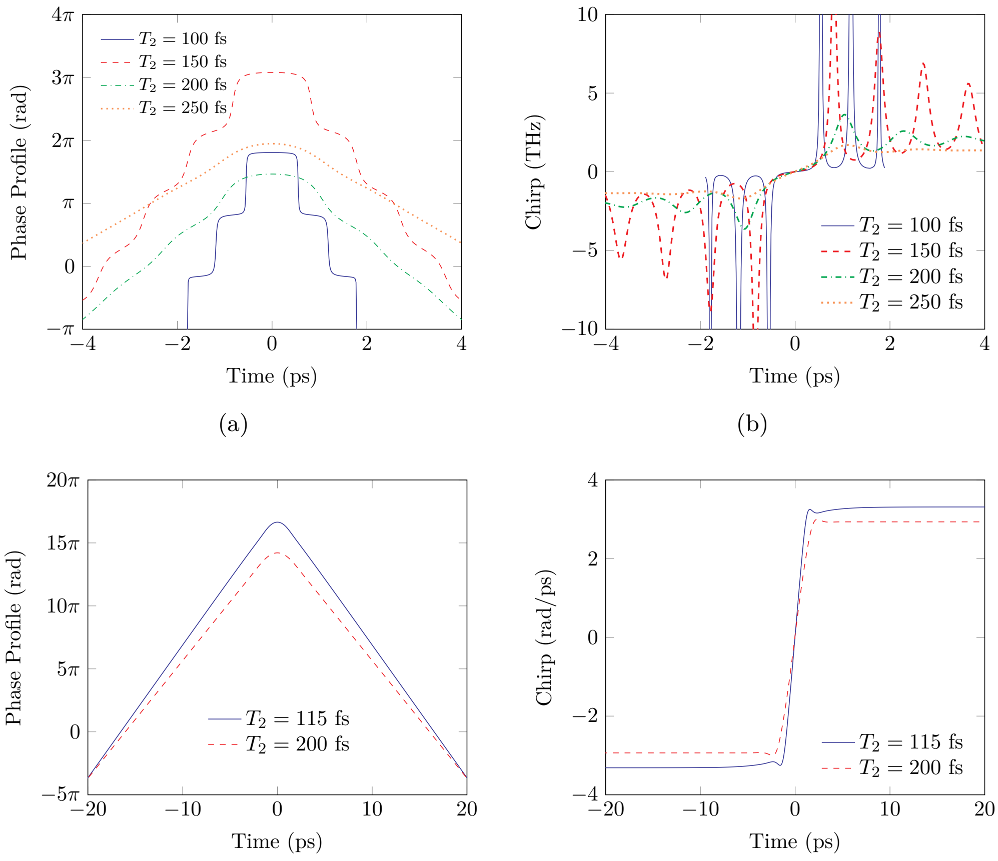

(a)

(b)

(c)

(d)

Figure 4.6: (a), (c) Phase profiles and (b), (d) chirp of the pulses for different values of T_2, for $\beta_4 = -0.080$ ps^{4}m^{-1}, $P_{\text{sat}} = 3$ W and $g_0 = 1.36$ m^{-1} (top row) and $\beta_4 = 0.080$ ps^{4}m^{-1}, $P_{\text{sat}} = 80$ W and $g_0 = 1.48$ m^{-1} (bottom row). In all cases, $\beta_2 = 0$.

Likewise, the spectral shape is also influenced by T_2. When 4OD is negative (Figs. 4.7(a) and 4.7(b), in linear and logarithmic scale respectively), the T_2 increase leads to a progressive narrowing of the spectrum and the top becomes less and less flat, due to the absence of the oscillations. As for positive 4OD (Figs. 4.7(c) and 4.7(d), linear and logarithmic scale respectively), the differences are clearer. When $T_2 = 115$ fs, the pulse takes a similar shape as the one shown in Fig. 4.4 for $\beta_4 > 0$, with two peaks at the edges of the spectrum. With $T_2 = 200$ fs, the spectrum becomes bell-shaped and the side peaks are no longer present. Interestingly, the peak of the spectrum for $T_2 = 200$ fs has a very similar shape to the middle section of the spectrum for $T_2 = 115$ fs. In fact, in logarithmic scale (Fig. 4.7(d)), the top of both spectra only differs in the presence of the peaks at the edges.

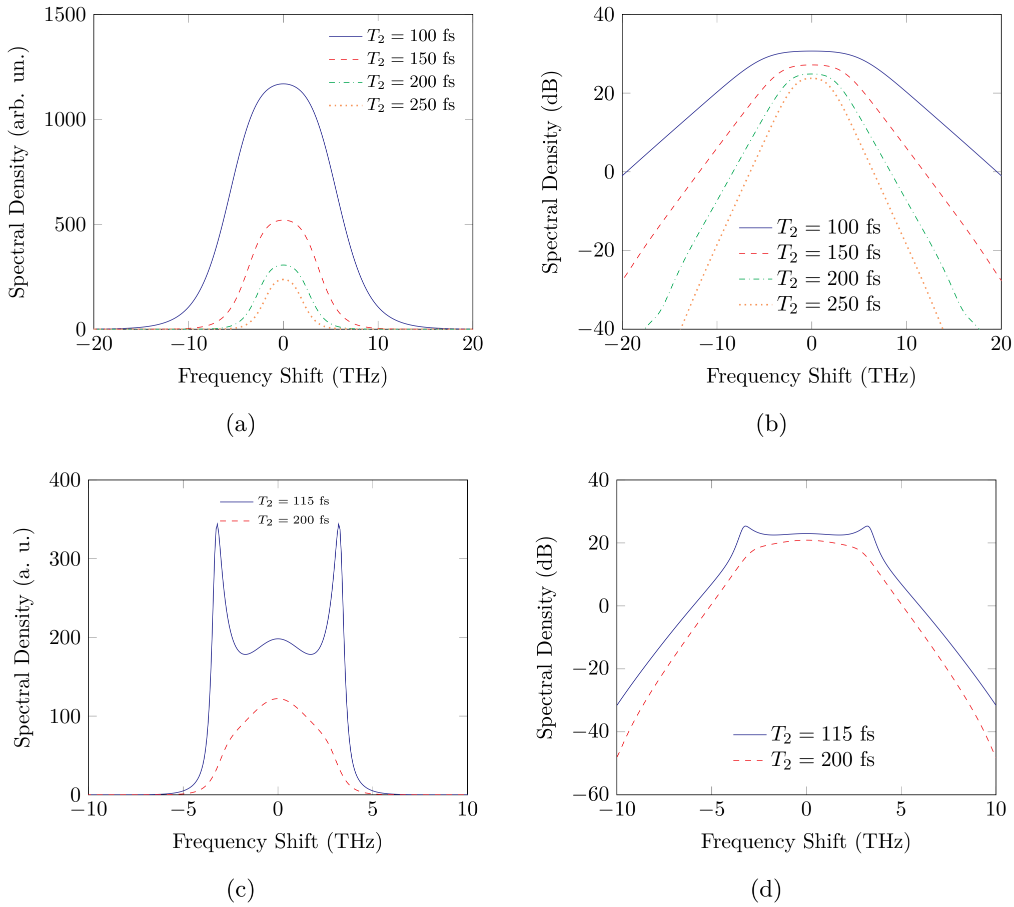

Figure 4.7: Pulse spectra for varying T_2 in (a), (c) linear and (b), (d) logarithmic scale, for negative (top row) and positive (bottom row) 4OD. Parameters: $\beta_2 = 0$, $\beta_4 = \pm 0.080$ ps^{4}m^{-1}, $g_0 = 1.36$ m^{-1}, $P_{\text{sat}} = 3$ W.

4.2 Energy-Width Scaling

To design a mode-locked fiber laser capable of emitting high energy ultrashort pulses, it is essential to find how the different laser parameters impact the pulse energy and width. Before studying the dependence with g_0, P_{sat} and T_2, it is first important to understand how the energy of the pulses varies with the 4OD parameter. To do so, g_0, T_2 and P_{sat} were kept constant, with values of 1.45 m^{-1}, 100 fs and 80 W, respectively, and β_4 was arbitrarily varied from -0.12 ps^{4}m^{-1} to 0.12 ps^{4}m^{-1}, using $\beta_2 = -0.024$ ps^{2}m^{-1} in order to allow the zero 4OD transition. The pulse energy, E, given by,

$$E = \int |W|^2 dT, \tag{4.1}$$

was calculated by evaluating the integral with a trapezoidal method, while the pulse width was calculated as the full width at half maximum (FWHM) of $|W|^2$.

The influence of β_4 on the pulse width and energy is represented in Fig. 4.8. The energy of pulses (Fig. 4.8(a)) grows linearly, with $|\beta_4|$, with the growth rate being much greater for negative 4OD. In contrast, the pulse width (Fig. 4.8(b)) increases with β_4, but the growth rate is now much slower for negative β_4. The inset in Fig. 4.8(b) shows that changing β_4 from -0.12 to 0 ps^{4}m^{-1} resulted in a width increase of approximately 9%, whereas changing β_4 from 0 to 0.12 ps^{4}m^{-1} led to a width increase close to 350% . Therefore, these results evidence that the pulses with the highest energies (in the nJ range) as well as the shortest widths (in the range of a few 100 ns) are found for negative 4OD. This information is encompassed in Fig. 4.8(c), where the dependence of the energy with the width is represented, showing a very sharp decrease when $\beta_4 < 0$ (blue solid curve), subsequently increasing when $\beta_4 > 0$ (dashed red curve).

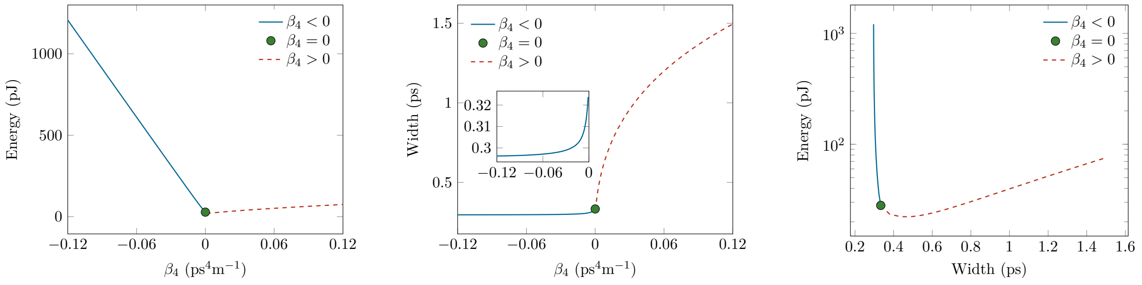

(a) (b) (c)

Figure 4.8: Energy and width dependence on the 4OD parameter. (a) Energy dependence with β_4. (b) Width dependence with β_4. The inset highlights the depencence of the width with negative 4OD. (c) Energy-width curve when β_4 is swept from negative to positive values. Parameters: $\beta_2 = -0.024$ ps^{2}m^{-1}, $g_0 = 1.45$m^{-1}, $T_2 = 100$ fs and $P_{\text{sat}} = 80$ W

To study the impact the g_0, P_{sat} and T_2 parameters have on the energy and width of pulses, the dispersion coefficients were kept constant, taking $\beta_2 = 0$ and $|\beta_4| = 0.080$ ps^{4}m^{-1}. Only the sign of β_4 was allowed to change to distinguish between the effects of positive and negative 4OD. Fig. 4.9 thus shows the dependence of the energy with g_0, P_{sat} and T_2, for $\beta_4 < 0$ (Figs. 4.9(a), 4.9(b), 4.9(c), respectively) and $\beta_4 > 0$ (Figs. 4.9(d), 4.9(e) and 4.9(f), respectively). Parameter regions were chosen so that localized solutions of Eq. (2.28) exist and propagate stably. In fact if g_0 is too low or either T_2 or P_{sat} are too high, stationary soliton solutions of the evolution equation do not exist. In contrast, if g_0 is too high, or if P_{sat} or T_2 are too low, solutions are unstable. It immediately becomes apparent that the energy is much larger for negative 4OD than for positive 4OD, further reinforcing the results from Fig. 4.8. As an example, for $g_0 = 1.45$ m^{-1}, the energy for $\beta_4 < 0$ is about 15 times greater than the one calculated for the same g_0 but with positive 4OD. More striking is the case of the energy dependence with T_2, where energy values are about two orders of magnitude greater for $\beta_4 < 0$ than for $\beta_4 > 0$, for the same T_2 value. In terms of the influence of the parameters themselves on the energy, an increase in g_0 leads to an increment in the energy, while increasing P_{sat} and T_2 (in most cases) leads to an energy decrease, for either positive or negative 4OD. In fact, higher g_0 corresponds to higher gain and higher P_{sat} to higher losses, thus justifying the respective energy trends. The dependence with T_2 however is not as straightforward to interpret, because the $E - T_2$ trend when $\beta_4 < 0$ has some nuances that require further inspection. When higher saturation powers (80 W and 160 W for example) are used, the energy strictly decreases with T_2 but stable solutions only exist for a shorter range of T_2 values (see inset in Fig. 4.9(c)) than when a lower saturation power such as 3 W is used. In this case, for $T_2 \gtrsim 250$ fs, i.e., when pulse profiles become hyperbolic secant shaped, the energy actually starts to increase slowly with T_2.

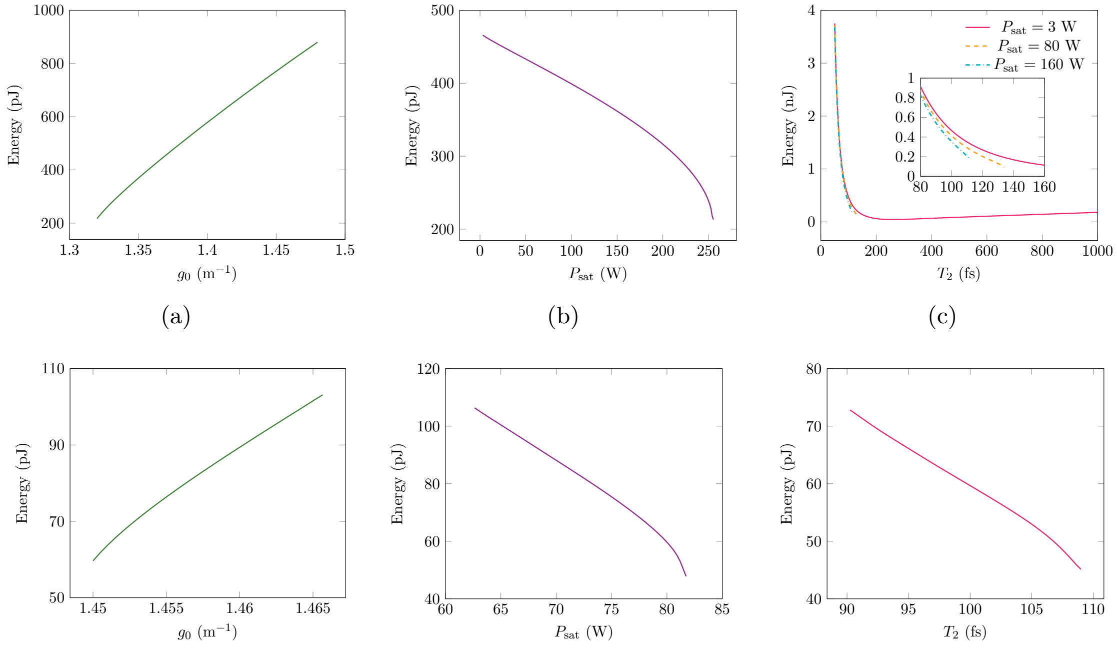

(a) (b) (c)

(d) (e) (f)

Figure 4.9: Energy dependence with g_0 (left column), P_{sat} (middle column) and T_2 (right column) for $\beta_4 = -0.080$ ps^{4}m^{-1} (top row) and $\beta_4 = 0.080$ ps^{4}m^{-1} (bottom row). When kept constant, $P_{\text{sat}} = 80$ W and $T_2 = 100$ fs for either 4OD value, while g_0 took values of 1.36 m^{-1} when $\beta_4 < 0$ and of 1.45 m^{-1} when $\beta_4 > 0$.

In terms of the soliton temporal width, its dependence on the g_0, P_{sat} and T_2 parameters is plotted for negative 4OD in Figs. 4.10(a), 4.10(b) and 4.10(c), respectively, and for positive 4OD in the same order in Figs. 4.10(d), 4.10(e) and 4.10(f). In the same way that the pulse energy is greatest when $\beta_4 < 0$, the pulse width is also the lowest in this dispersion regime, once again reinforcing the idea that the highest energy ultrashort pulses are generated with negative 4OD rather than positive. It is also apparent that the width decreases with g_0 and increases with P_{sat} and T_2. In the latter case, even for $P_{\text{sat}} = 3$ W, the width increases in all of the T_2 range, and the width difference for the saturation powers of 3 W, 80 W and 160 W is emphasized in the inset in Fig. 4.10(c). The monotonous increase of the width with T_2 is not surprising however, since this parameter is directly related to the spectral bandwidth. An increase in T_2 leads to a reduction in the spectral bandwidth and thus to greater pulse widths.

Combining the results from Figs. 4.9 and 4.10, yields the energy-width trend of quartic solitons of the distributed model, presented in Fig. 4.11. For negative 4OD (Fig. 4.11(a)), it

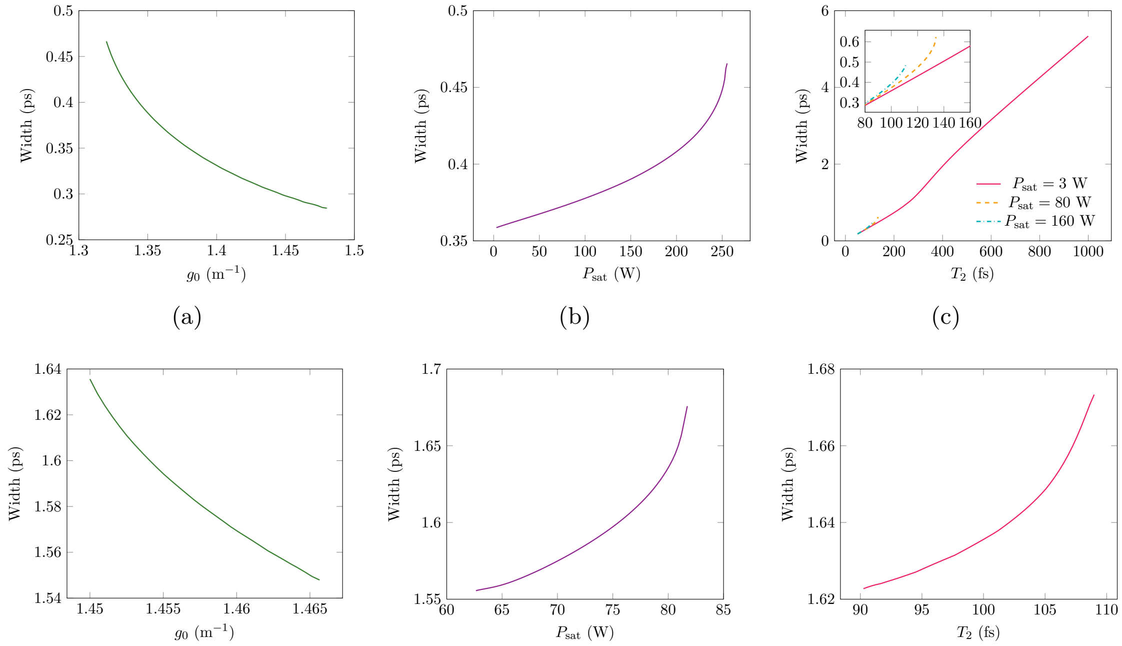

(a) (b) (c)

(d) (e) (f)

Figure 4.10: Width dependence with g_0 (left column), $P_{\rm sat}$ (middle column) and T_2 (right column) for $\beta_4 = -0.080$ ps^{4}m^{-1} (top row) and $\beta_4 = 0.080$ ps^{4}m^{-1} (bottom row). When kept constant, $P_{\rm sat} = 80$ W and $T_2 = 100$ fs for either 4OD value, while g_0 took values of 1.36 m^{-1} when $\beta_4 < 0$ and of 1.45 m^{-1} when $\beta_4 > 0$.

was found that, in most cases, the energy scales inversely with the width cubed, following the trend already predicted for pure-quartic solitons (PQSs) in other models [37, 39, 43]. The only exception is the $E - w_0$ curve obtained in a T_2 sweep for $P_{\rm sat} = 3$ W, where a non-monotonic trend is found instead. Nevertheless, for $w_0 \lesssim 0.7$ ps, i.e., $T_2 \lesssim 250$ fs, the energy does scale with w_0^{-3}, starting to increase linearly with the width after this point (fit in Fig. 4.11(a)). Interestingly, most of the energy-width points found for $\beta_4 < 0$ fall approximately in the same $E \propto w_0^{-3}$ curve. Through curve fittings (see gray dashed line), the curve was found to be defined as $E = 21.5 w_0^{-3}$. Recalling Eq. (1.2), Tam *et al.* [39] found that PQSs follow the approximate relation,

$$E \approx 2.87 \frac{|\beta_4|}{\gamma w_0^3}. \tag{4.2}$$

In the case of the distributed model, the effective nonlinear parameter, $\bar{\gamma}$, needs to be considered. Although according to Eq. (2.27), $\bar{\gamma}$ varies with this parameter, in the considered g_0 range, for all simulations, it was found that $\bar{\gamma} \approx 0.010$ W^{-1}m^{-1}, never deviating from this value significantly. Using this constant value the calculated slope of 21.5, when $\beta_4 < 0$ the energy-width scaling of dissipative quartic solitons is approximately described by

$$E \approx 2.69 \frac{|\beta_4|}{\bar{\gamma} w_0^3}. \tag{4.3}$$

This relation is actually very close to Eq. (4.2), that refers to conservative quartic solitons.

When it comes to positive 4OD however (Fig. 4.11(b)), it is immediately clear that the $E \propto w_0^3$ relation reported in [46] is not followed, since the energy strictly decreases with the width in all three parameter sweeps. To characterize the trends of these energy-width curves, fits of the data to functions of the type aw_0^b were attempted (see dashed lines in Fig. 4.11(b)), where a and b are fitting coefficients, and it was concluded that the $E \propto w_0^{-3}$ relation is not verified in any of the sweeps. Furthermore, it is also apparent that when $\beta_4 > 0$, the energy-width behavior is dependent on the parameter that was swept, since the data does not fit over a single curve and, particularly for the sweeps of P_{sat} and T_2, aw_0^b functions do not seem to be the most accurate models for the data. This is not the case for the g_0 sweep, where the energy-width curve can be defined by a $E \propto w_0^{-10}$ trend. Even though, theoretically, this scaling would be far more favorable than an energy scaling with the inverse third power of the width, as has been stressed, pulse energies with positive 4OD are much lower than for negative 4OD, and widths are also significantly greater, rendering this scaling impractical in ultrashort pulse applications.

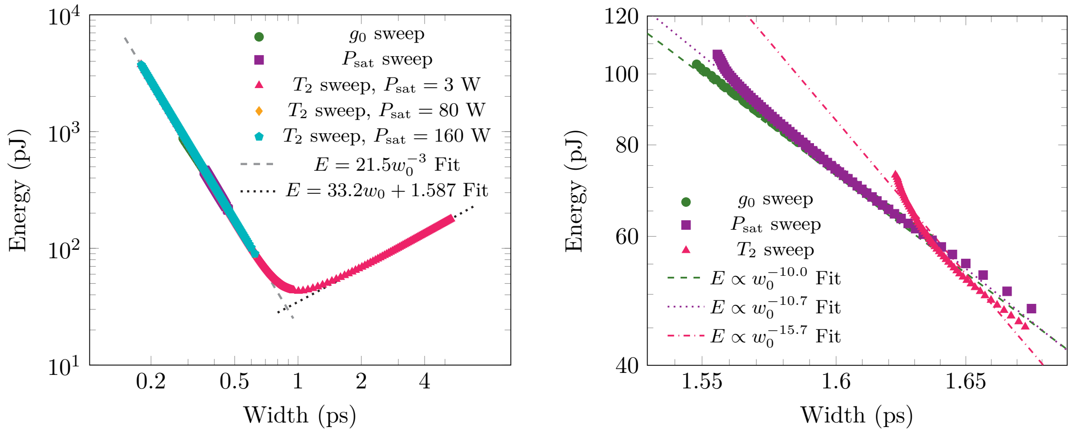

(a) (b)

Figure 4.11: Energy-width curves using $\log_{10}$ scale and associated fittings, obtained by sweeping g_0, P_{sat} and T_2 for (a) $\beta_4 = -0.080$ ps^{4}m^{-1} and (b). When kept constant, $T_2 = 100$ fs, $g_0 = 1.36$ m^{-1} for $\beta_4 < 0$ and 1.45 m^{-1} for $\beta_4 > 0$ and when not specified, $P_{\text{sat}} = 80$ W.

4.3 Energy Maximization

The results presented in the previous section indicate how a single parameter, g_0, P_{sat} or T_2 could be manipulated to maximize the energy of ultrashort quartic solitons, provided that the others were kept constant. Moreover, those results provide some insights on how changing specific parameters may yield a better outcome in the maximization of the energy. For example, it was with the sweep of T_2 (Fig. 4.9(c)) that the highest energies were found, reaching values of a few nJ and even though the energy is lower for higher P_{sat} values, increasing this parameter from 3 W, to 80 W and further so to 160 W (see inset) did not lead to a very significant energy reduction. Therefore, the generation of pulses with higher energies will inevitably involve a compromise in the choice of parameters. As a thought experiment, a reduction of T_2 in relation to the minimum value in Fig. 4.9(c), could lead to a further increase in the energy. However, to find stable solutions in that T_2 region, hypothetically, an increase in P_{sat} or even a reduction in g_0 could be necessary, but the benefits to the energy of decreasing T_2 would ideally outweigh the drawbacks of increasing P_{sat} or reducing g_0. Hence, the maximization of the energy must take into account the simultaneous variation of all parameters.

The problem with varying g_0, P_{sat} and T_2 simultaneously is that the existence and stability of solutions of Eq. (2.28) is strongly dependent on the working parameter region. In fact, an increase of P_{sat} implies that the saturable absorber (SA) saturates for higher power, leading to a decrease in the nonlinear gain. In turn, the other losses might be left unbalanced and soliton solutions will not be found. This same effect also occurs when g_0 is decreased which, according to Eq. (2.27), results in greater effective saturation powers, $\bar{P}_{\text{sat}}$. For higher g_0 values, the linear losses $(-g_0/2 + k_{\text{OC}}/2L + M/2L)$ tend to zero, and the linear gain would produce unstable background. On the other hand, lower values of P_{sat} lead to a sharp, unbalanced, increase in the nonlinear gain, also leading to unstable solitons

To have a better understanding on how highly energetic ultrashort pulses can be generated through the combination of the aforementioned parameters, solutions were searched for on a $g_0 - T_2$ region for saturation powers of 80 W and 160 W, considering $\beta_2 = 0$ and $\beta_4 = -0.080$ ps^{4}m^{-1}. Negative 4OD was considered because, so far, all results stress that the shortest pulses and also the most energetic ones are found in this dispersion regime. The stability eigenvalues of these solutions were calculated using the method described in Section 3.3, since it is a much faster approach than the direct integration of the evolution equation through the pseudo-spectral method.

Fig. 4.12 shows the stability border of the solutions in the $g_0 - T_2$ plane, for $P_{\text{sat}} = 80$ W (Figs. 4.12(a) and 4.12(b)) and $P_{\text{sat}} = 160$ W (Fig. 4.12(c) and 4.12(d)) with the energy in nJ in logarithmic scale (left column) and the width in fs (right column) being represented as a contour plot. It is important to stress that in spite of the energy increasing with g_0 for constant T_2 and P_{sat}, lower values of g_0 allow stable solutions to exist for lower values of T_2, thus causing a significant increase in the energy. Likewise, and although for constant T_2 and g_0 a decrease in P_{sat} represents an increase in the energy, if T_2 and g_0 are allowed to vary, the contribution from these changes will compensate the negative contribution of a higher value of P_{sat}, yielding greater energies. In terms of the pulse widths, it has been shown in Fig. 4.10(c), and is further reinforced in Figs. 4.12(b) and 4.12(d), that as T_2 decreases, the pulse width also decreases, due to T_2 being a parameter related to the spectral filtering, thus having a direct impact in the pulse shape and width, which always changes in the same direction as the referred parameter. As a result, the highest energy pulses are also the shortest ones. In fact, setting $T_2 = 8$ fs and $g_0 = 1.30$ m^{-1}, yielded quartic solitons with an energy of 391 nJ and a width of 39 fs. These energy values far surpass the ones presented in previous works on quartic solitons [39, 42, 43, 46].

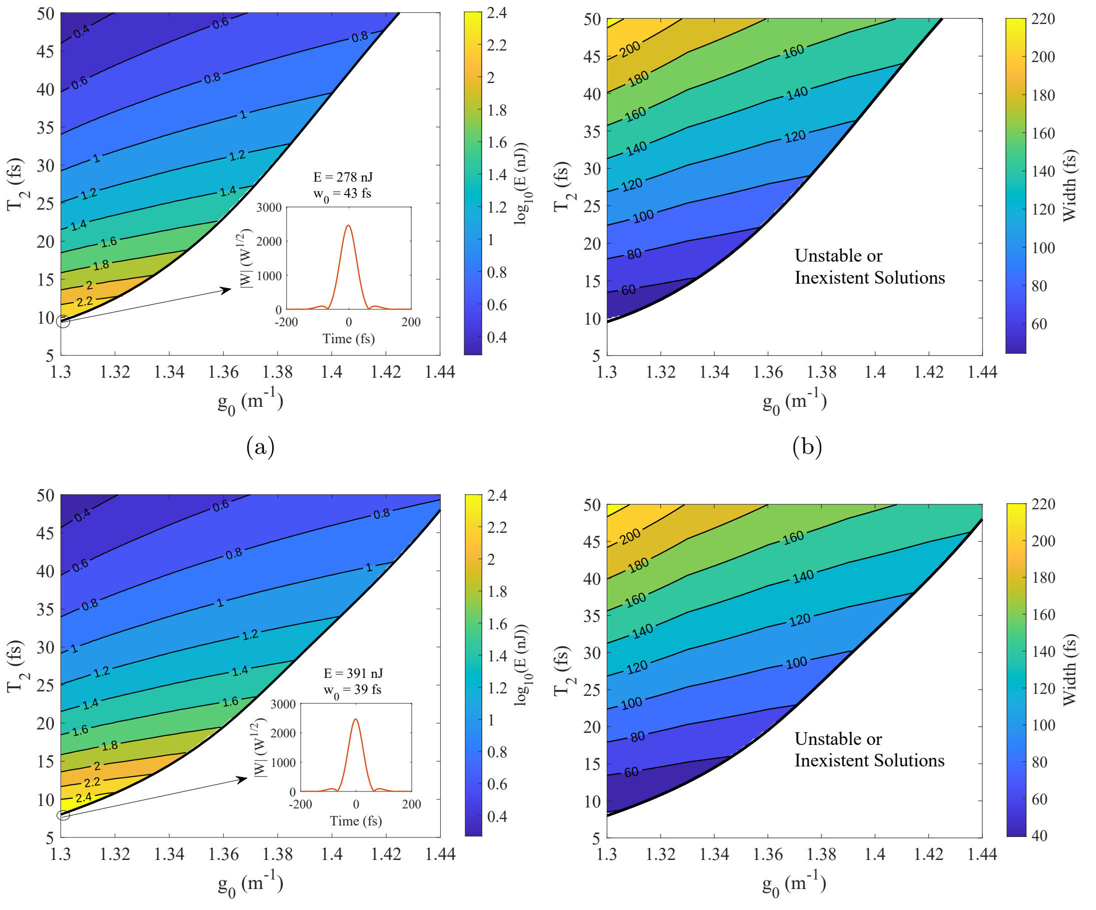

(a) (b)

(c) (d)

Figure 4.12: Region of existence of stable solitons in the $g_0 - T_2$ plane. In the colored regions, solutions exist and propagate steadily. The base 10 logarithm of the energies in nJ ((a) and (c)) and the widths in fs ((a) and (b)) are represented as contour plots, for $P_{\text{sat}} = 80$ W (top row) and $P_{\text{sat}} = 160$ W (bottom row). For each saturation power, the insets show the highest energy pulses found within the stability border, displaying the corresponding energy and width values. Dispersion parameters: $\beta_2 = 0$, $\beta_4 = -0.08$ ps^{4}m^{-1}.

For the sake of comparison, a similar procedure was followed but for $\beta_4 = 0.080$ ps^{4}m^{-1} and $P_{\text{sat}} = 80$ W instead, with the resulting stability regions and contour plots of the energy and width being represented in Figs. 4.13(a) and 4.13(b) respectively. Even through the simultaneous variation of g_0 and T_2 for fixed P_{sat}, solutions with energies higher than the ones in Fig. 4.11(b) were not found. This is due to the fact that the parameter region where stable soliton solutions exist for positive 4OD is far more limited than the one found with negative 4OD. Moreover, by comparing the results in Figs. 4.12 and 4.13 it is noticeable that the highest energy and shortest width pulses for negative 4OD are about 3 orders of magnitude larger than the ones for positive 4OD. Therefore, mode-locked lasers with positive 4OD seem not to be the best option whenever the practical application requires very energetic short pulses.

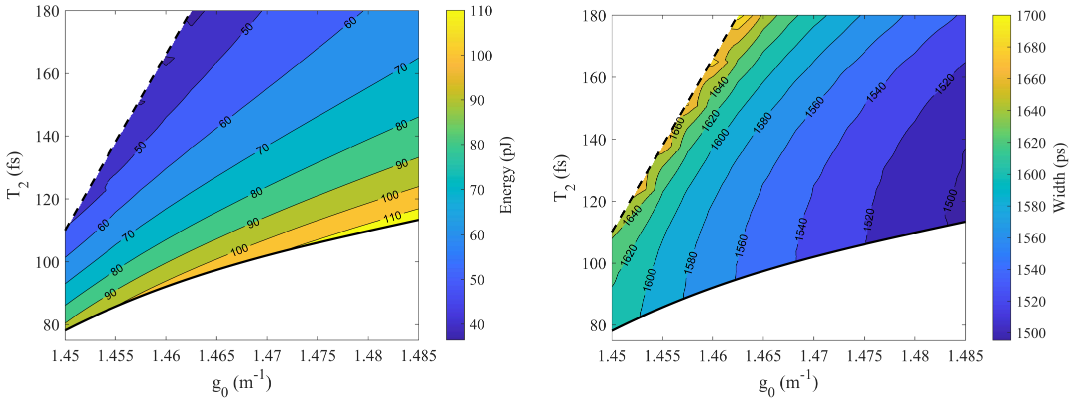

(a)

(b)

Figure 4.13: Region of existence of stable solitons in the $g_0 - T_2$ plane. The energy in pJ (a) and the width in ps (b) are represented above the curves as contour plots. Equation parameters: $\beta_2 = 0$, $\beta_4 = 0.08$ ps^{4}m^{-1} and $P_{\text{sat}} = 80$ W.

5. Conclusions and Future Work

In recent years, quartic solitons have gained interest in the fields of optical Kerr cavities and mode-locked lasers, because the energy of such pulses scales inversely with the width cubed. This is of particular importance in applications such as nonlinear medical imaging and material processing as well as frequency comb and supercontinuum generation. Even though conservative quartic solitons have been studied rather extensively, contradicting results on dissipative quartic solitons may evidence that this energy-width scaling is not universally valid. Thus, further investigation was needed to clarify the origin of these differing results and to understand how different physical parameters could influence this trend.

In this dissertation, a distributed model for a passively mode-locked fiber laser was used to further explore the energy-width scaling of quartic dissipative solitons, to verify the parameter dependence of this trend and to find ways to maximize the energy of ultrashort pulses. The model was carefully chosen to include second order dispersion (2OD) and fourth order dispersion (4OD), to not approximate the saturable absorber (SA) term and finally to allow for a direct correspondence between equation parameters and realistic laser data. Localized solutions of the distributed equation were found using the Newton conjugate-gradient (NCG) method. These were subsequently perturbed and taken as inputs in the integration of the distributed equation using a pseudo-spectral method, to verify their stability and study their evolution along the spatial coordinate. Finally, a linear stability analysis was undertaken to map the parameter region where stable soliton solutions exists, and to aid in the search for maximum energy solitons.

Quartic soliton solutions were found for both positive and negative 4OD, in the presence or in the absence of positive and negative 2OD, in a range of 4OD dispersion (β_4), gain (g_0) saturation power (P_{sat}) and spectral filtering (T_2) parameters. The pulse shape varied with both β_4 and T_2. For $T_2 \lesssim 200$ fs (weak filtering), negative 4OD resulted in Gaussian pulses with oscillating tails, while hyperbolic secant pulses sitting upon a broad pedestal with exponentially decaying tails were found for positive 4OD. When $T_2 \gtrsim 200$ fs (strong filtering), hyperbolic secant pulses were obtained, for either sign of β_4. In all of these cases, soliton solutions had a non-uniform phase profile, leading to frequency chirping, which is directly related to the energy inflow and outflow due to the presence of gain and loss mechanisms. Under strong filtering, the pulse spectra were bell shaped curves for either sign of 4OD, but with weak filering and $\beta_4 < 0$, pulse oscillations led to a flatter spectral peak, while $\beta_4 > 0$ resulted in spectra with two lateral peaks.

Pulse energies (E) were found to be greater and pulse widths (w_0) shorter in the negative 4OD regime, with the energy increasing with $|\beta_4|$. Pulse energy increased with g_0 and decreased with P_{sat}, since these terms are related to energy gain and loss respectively. For positive 4OD, the energy decreased with T_2 and this same behaviour occured for negative 4OD but only for $T_2 \lesssim 200$ fs. After this point the energy started to increase with T_2, yielding a non-monotonous trend. The width followed an opposite trend as the energy with both g_0 and P_{sat}, and it decreased monotonically for all values of T_2, regardless of the sign of β_4.

In the negative 4OD regime and under weak filtering, the energy scaled inversely with the third power of the width, following a trend very similar to the one found in conservative quartic solitons, for all parameter sweeps. When g_0 and P_{sat} were kept constant and T_2 was increased beyond 200 fs, the energy increased with the width instead, however. In contrast, a trend that described the $E - w_0$ curve when $\beta_4 > 0$ for all the parameter sweeps was not found, but the energy strictly decreased with the width in all cases. Therefore, the $E \propto w_0^3$ relation reported in [46] was not found, and the results present in this work evidence that in the dissipative case, the $E - w_0$ is indeed parameter dependent, at least in the case of $\beta_4 > 0$.

With both the energy and stability of solutions being strongly parameter dependent, a careful compromise in the choice of g_0, P_{sat} and T_2 values (assuming fixed dispersion) is of utmost importance to maximize the energy. Despite the energy being greater for higher g_0 and lower P_{sat}, as long as T_2 is allowed to decrease, it was found that the resulting energy increase from this reduction far outweighs the negative contribution of a g_0 decrease or a P_{sat} increase. Through a linear stability analysis, quartic solitons with an energy of 391 nJ and a width of 39 fs were found, considering $g_0 = 1.30\ \mathrm{m}^{-1}$, $P_{\mathrm{sat}} = 160$ W and $T_2 = 8$ fs, with $\beta_4 = -0.080\ \mathrm{ps}^4\mathrm{m}^{-1}$. It is thus possible to conclude that the manipulation of the spectral filtering in a realistic laser setup will be the key to maximize the energy of generated pulses while simultaneously decreasing the width, under the presence of negative 4OD. Energies are orders of magnitude lower under positive 4OD so, in practice, it is advantageous to use $\beta_4 < 0$.

As future work, the internal energy flow of the quartic soliton solutions of the distributed model can be quantified. Besides, solutions were found for different parameter values which had the same energy and width, and differences between these solutions could be investigated. Furthermore, the model itself can be improved by the addition of a gain saturation term. It can be used also to study other interesting effects such as modulation instability [49] and to search for oscillating solutions [44]. Moreover, it is also relevant to understand how larger values of the 2OD parameter how the presence of a third order dispersion (3OD) term could impact the results. Finally, this work can be expanded by transcribing it to a lumped model, which will allow the evaluation of the accuracy of the distributed model through the comparison of solutions obtained in both approaches.

References

[1] J. S. Russel, “Report on waves”, in *Report of the Fourteenth Meeting of the British Association for the Advancement of Science*, pp. 311–390, London: John Murray, 1884.

[2] N. J. Zabusky and M. D. Kruskal, “Interaction of "solitons" in a collisionless plasma and the recurrence of initial states”, *Physical Review Letters*, vol. 15, no. 6, pp. 240–243, 1965. DOI: `10.1103/physrevlett.15.240`.

[3] G. P. Agrawal, *Nonlinear Fiber Optics*, 3rd ed. Academic Press, 2001.

[4] C. M. de Sterke, A. F. J. Runge, D. D. Hudson, and A. Blanco-Redondo, “Pure-quartic solitons and their generalizations—theory and experiments”, *APL Photonics*, vol. 6, no. 9, p. 091 101, 2021. DOI: `10.1063/5.0059525`.

[5] P. Grelu and N. Akhmediev, “Dissipative solitons for mode-locked lasers”, *Nature Photon*, vol. 6, pp. 8492, 2012. DOI: `10.1038/nphoton.2011.345`.

[6] J. M. Dudley, G. Genty, A. Mussot, A. Chabchoub, and F. Dias, “Rogue waves and analogies in optics and oceanography”, *Nature Reviews Physics*, vol. 1, no. 11, pp. 675–689, 2019. DOI: `10.1038/s42254-019-0100-0`.

[7] H. Kuwayama and S. Ishida, “Biological soliton in multicellular movement”, *Scientific Reports*, vol. 3, no. 1, 2013. DOI: `10.1038/srep02272`.

[8] J. W. Rottman and R. Grimshaw, “Atmospheric internal solitary waves”, in *Environmental Stratified Flows*, pp. 61–88, Kluwer Academic Publishers, 2002. DOI: `10.1007/0-306-48024-7\_3`.

[9] L. M. Aycock, H. M. Hurst, D. K. Efimkin, D. Genkina, H.-I. Lu, V. M. Galitski, and I. B. Spielman, “Brownian motion of solitons in a Bose–Einstein condensate”, *Proceedings of the National Academy of Sciences*, vol. 114, no. 10, pp. 2503–2508, 2017. DOI: `10.1073/pnas.1615004114`.

[10] M. Vukcevic, “Soliton structures in different astrophysical systems”, *The European Physical Journal D*, vol. 75, no. 3, 2021. DOI: `10.1140/epjd/s10053-021-00082-y`.

[11] A. Hasegawa and F. Tappert, “Transmission of stationary nonlinear optical pulses in dispersive dielectric fibers. i. anomalous dispersion”, *Applied Physics Letters*, vol. 23, no. 3, pp. 142–144, 1973. DOI: `10.1063/1.1654836`.

[12] L. F. Mollenauer, R. H. Stolen, and J. P. Gordon, “Experimental observation of picosecond pulse narrowing and solitons in optical fibers”, *Physical Review Letters*, vol. 45, no. 13, pp. 1095–1098, 1980. DOI: `10.1103/physrevlett.45.1095`.

[13] G. P. Agrawal, *Fiber-Optic Communication Systems*, 3rd ed. John Wiley & Sons, 2002.

[14] H. A. Haus and W. S. Wong, “Solitons in optical communications”, *Reviews of Modern Physics*, vol. 68, no. 2, pp. 423–444, 1996. DOI: `10.1103/revmodphys.68.423`.

[15] D. E. Spence, P. N. Kean, and W. Sibbett, “60-fsec pulse generation from a self-mode-locked ti:sapphire laser”, *Optics Letters*, vol. 16, no. 1, p. 42, 1991. DOI: `10.1364/ol.16.000042`.

[16] I. D. Jung, F. X. Kärtner, N. Matuschek, D. H. Sutter, F. Morier-Genoud, G. Zhang, U. Keller, V. Scheuer, M. Tilsch, and T. Tschudi, “Self-starting 65-fs pulses from a ti:sapphire laser”, *Optics Letters*, vol. 22, no. 13, p. 1009, 1997. DOI: `10.1364/ol.22.001009`.

[17] A. H. Zewail, “Femtochemistry. past, present, and future”, *Pure and Applied Chemistry*, vol. 72, no. 12, pp. 2219–2231, 2000. DOI: `10.1351/pac200072122219`.

[18] G. Raciukaitis, “Ultra-short pulse lasers for microfabrication: A review”, *IEEE Journal of Selected Topics in Quantum Electronics*, vol. 27, no. 6, pp. 1–12, 2021. DOI: `10.1109/jstqe.2021.3097009`.

[19] W. Knox, “Ultrafast technology in telecommunications”, *IEEE Journal of Selected Topics in Quantum Electronics*, vol. 6, no. 6, pp. 1273–1278, 2000. DOI: `10.1109/2944.902178`.

[20] W. Sibbett, A. A. Lagatsky, and C. T. A. Brown, "The development and application of femtosecond laser systems", *Optics Express*, vol. 20, no. 7, p. 6989, 2012. DOI: `10.1364/oe.20.006989`.

[21] N. Akhmediev, J. Soto-Crespo, and P. Grelu, "Roadmap to ultra-short record high-energy pulses out of laser oscillators", *Physics Letters A*, vol. 372, no. 17, pp. 3124–3128, 2008. DOI: `10.1016/j.physleta.2008.01.027`.

[22] M. Andreana, T. Le, W. Drexler, and A. Unterhuber, "Ultrashort pulse Kagome hollow-core photonic crystal fiber delivery for nonlinear optical imaging", *Opt. Lett.*, vol. 44, no. 7, pp. 1588–1591, 2019. DOI: `10.1364/OL.44.001588`.

[23] N. Nishizawa, Y. Chen, P. Hsiung, E. P. Ippen, and J. G. Fujimoto, "Real-time, ultrahigh-resolution, optical coherence tomography with an all-fiber, femtosecond fiber laser continuum at 1.5 µm", *Opt. Lett.*, vol. 29, no. 24, pp. 2846–2848, 2004. DOI: `10.1364/OL.29.002846`.

[24] J. M. Dudley, G. Genty, and S. Coen, "Supercontinuum generation in photonic crystal fiber", *Reviews of Modern Physics*, vol. 78, no. 4, pp. 1135–1184, 2006. DOI: `10.1103/revmodphys.78.1135`.

[25] S. T. Cundiff and J. Ye, "Colloquium: Femtosecond optical frequency combs", *Rev. Mod. Phys.*, vol. 75, pp. 325–342, 1 2003. DOI: `10.1103/RevModPhys.75.325`.

[26] K. J. Blow, N. J. Doran, and D. Wood, "Generation and stabilization of short soliton pulses in the amplified nonlinear schrödinger equation", *Journal of the Optical Society of America B*, vol. 5, no. 2, p. 381, 1988. DOI: `10.1364/josab.5.000381`.

[27] H. A. Haus, J. D. Moores, and L. E. Nelson, "Effect of third-order dispersion on passive mode locking", *Optics Letters*, vol. 18, no. 1, p. 51, 1993. DOI: `10.1364/ol.18.000051`.

[28] A. Höök and M. Karlsson, "Ultrashort solitons at the minimum-dispersion wavelength: Effects of fourth-order dispersion", *Optics Letters*, vol. 18, no. 17, p. 1388, 1993. DOI: `10.1364/ol.18.001388`.

[29] Y. Kodama, M. Romagnoli, M. Midrio, and S. Wabnitz, "Role of third-order dispersion on soliton instabilities and interactions in optical fibers", *Optics Letters*, vol. 19, no. 3, p. 165, 1994. DOI: `10.1364/ol.19.000165`.

[30] M. Karlsson and A. Höök, "Soliton-like pulses governed by fourth order dispersion in optical fibers", *Optics Communications*, vol. 104, no. 4, pp. 303–307, 1994. DOI: `10.1016/0030-4018(94)90560-6`.

[31] V. I. Kruglov and J. D. Harvey, "Solitary waves in optical fibers governed by higher-order dispersion", *Phys. Rev. A*, vol. 98, p. 063 811, 6 2018. DOI: `10.1103/PhysRevA.98.063811`.

[32] N. Akhmediev, A. Buryak, and M. Karlsson, "Radiationless optical solitons with oscillating tails", *Optics Communications*, vol. 110, no. 5-6, pp. 540–544, 1994. DOI: `10.1016/0030-4018(94)90246-1`.

[33] I. P. Christov, M. M. Murnane, H. C. Kapteyn, J. Zhou, and C.-P. Huang, "Fourth-order dispersion-limited solitary pulses", *Opt. Lett.*, vol. 19, no. 18, pp. 1465–1467, 1994. DOI: `10.1364/OL.19.001465`.

[34] A. Buryak and N. Akhmediev, "Stability criterion for stationary bound states of solitons with radiationless oscillating tails.", *Physical Review. E*, vol. 51 4, pp. 3572–3578, 1995. DOI: `10.1103/physreve.51.3572`.

[35] M. Piché, J.-F. Cormier, and X. Zhu, "Bright optical soliton in the presence of fourth-order dispersion", *Optics Letters*, vol. 21, no. 12, p. 845, 1996. DOI: `10.1364/ol.21.000845`.

[36] S. Roy and F. Biancalana, "Formation of quartic solitons and a localized continuum in silicon-based slot waveguides", *Phys. Rev. A*, vol. 87, p. 025 801, 2 2013. DOI: `10.1103/PhysRevA.87.025801`.

[37] A. Blanco-Redondo, C. M. de Sterke, J. Sipe, T. F. Krauss, B. J. Eggleton, and C. Husko, "Pure-quartic solitons", *Nature Communications*, vol. 7, no. 1, 2016. DOI: `10.1038/ncomms10427`.

[38] C.-W. Lo, A. Stefani, C. M. de Sterke, and A. Blanco-Redondo, "Analysis and design of fibers for pure-quartic solitons", *Optics Express*, vol. 26, no. 6, p. 7786, 2018. DOI: `10.1364/oe.26.007786`.

[39] K. K. K. Tam, T. J. Alexander, A. Blanco-Redondo, and C. M. de Sterke, “Stationary and dynamical properties of pure-quartic solitons”, *Optics Letters*, vol. 44, no. 13, p. 3306, 2019. DOI: `10.1364/ol.44.003306`.

[40] K. K. K. Tam, T. J. Alexander, A. Blanco-Redondo, and C. M. de Sterke, “Generalized dispersion kerr solitons”, *Physical Review A*, vol. 101, no. 4, 2020. DOI: `10.1103/physreva.101.043822`.

[41] C. Bao, H. Taheri, L. Zhang, A. Matsko, Y. Yan, P. Liao, L. Maleki, and A. E. Willner, “High-order dispersion in kerr comb oscillators”, *Journal of the Optical Society of America B*, vol. 34, no. 4, p. 715, 2017. DOI: `10.1364/josab.34.000715`.

[42] H. Taheri and A. B. Matsko, “Quartic dissipative solitons in optical kerr cavities”, *Optics Letters*, vol. 44, no. 12, p. 3086, 2019. DOI: `10.1364/ol.44.003086`.

[43] A. F. J. Runge, D. D. Hudson, K. K. K. Tam, C. M. de Sterke, and A. Blanco-Redondo, “The pure-quartic soliton laser”, *Nature Photonics*, vol. 14, no. 8, pp. 492–497, 2020. DOI: `10.1038/s41566-020-0629-6`.

[44] Z.-X. Zhang, M. Luo, J.-X. Chen, L.-H. Chen, M. Liu, A.-P. Luo, W.-C. Xu, and Z.-C. Luo, “Pulsating dynamics in a pure-quartic soliton fiber laser”, *Opt. Lett.*, vol. 47, no. 7, pp. 1750–1753, 2022. DOI: `10.1364/OL.454038`.

[45] A. F. J. Runge, T. J. Alexander, J. Newton, P. A. Alavandi, D. D. Hudson, A. Blanco-Redondo, and C. M. de Sterke, “Self-similar propagation of optical pulses in fibers with positive quartic dispersion”, *Optics Letters*, vol. 45, no. 13, p. 3365, 2020. DOI: `10.1364/ol.393835`.

[46] Z.-C. Qian, M. Liu, A.-P. Luo, Z.-C. Luo, and W.-C. Xu, “Dissipative pure-quartic soliton fiber laser”, *Optics Express*, vol. 30, no. 12, p. 22 066, 2022. DOI: `10.1364/oe.456929`.

[47] H. A. Haus, “Theory of mode locking with a fast saturable absorber”, *Journal of Applied Physics*, vol. 46, no. 7, pp. 3049–3058, 1975. DOI: `10.1063/1.321997`.

[48] H. Haus, J. Fujimoto, and E. Ippen, “Analytic theory of additive pulse and kerr lens mode locking”, *IEEE Journal of Quantum Electronics*, vol. 28, no. 10, pp. 2086–2096, 1992. DOI: `10.1109/3.159519`.

[49] J. M. Soto-Crespo, N. Akhmediev, and G. Town, “Continuous-wave versus pulse regime in a passively mode-locked laser with a fast saturable absorber”, *Journal of the Optical Society of America B*, vol. 19, no. 2, p. 234, 2002. DOI: `10.1364/josab.19.000234`.

[50] A. Zaviyalov, R. Iliew, O. Egorov, and F. Lederer, “Lumped versus distributed description of mode-locked fiber lasers”, *Journal of the Optical Society of America B*, vol. 27, no. 11, p. 2313, 2010. DOI: `10.1364/josab.27.002313`.

[51] D. Malheiro, M. Facão, and M. I. Carvalho, “Quartic solitons of a mode-locked laser distributed model”, *Optics Letters*, vol. 48, no. 21, pp. 5639–5642, 2023. DOI: `10.1364/ol.504202`.

[52] E. Hecht, *Optics*, 5th ed. Pearson Education, 2017.

[53] B. E. A. Saleh and M. C. Teich, *Fundamentals of Photonics*, 3rd ed. John Wiley & Sons, 2019.

[54] A. F. J. Runge, Y. L. Qiang, T. J. Alexander, M. Z. Rafat, D. D. Hudson, A. Blanco-Redondo, and C. M. de Sterke, “Infinite hierarchy of solitons: Interaction of kerr nonlinearity with even orders of dispersion”, *Physical Review Research*, vol. 3, no. 1, 2021. DOI: `10.1103/physrevresearch.3.013166`.

[55] R. L. Sutherland, *Handbook of Nonlinear Optics*, 2nd ed. Marcel Dekker, 2003.

[56] K. Okamoto, *Fundamentals of Optical Waveguides*, 2nd ed. Elsevier, 2006.

[57] M. Facão and M. I. Carvalho, “Existence and stability of solutions of the cubic complex ginzburg-landau equation with delayed raman scattering”, *Physical Review E*, vol. 92, no. 2, 2015. DOI: `10.1103/physreve.92.022922`.

[58] Y. S. KIshar and G. P. Agrawal, *Optical Solitons: From Fibers to Photonic Crystals*, 1st ed. Academic Press, 2003.

[59] P. K. A. Wai, H. H. Chen, and Y. C. Lee, "Radiations by "solitons" at the zero group-dispersion wavelength of single-mode optical fibers", *Physical Review A*, vol. 41, no. 1, pp. 426–439, 1990. DOI: `10.1103/physreva.41.426`.

[60] E. Picholle, C. Montes, C. Leycuras, O. Legrand, and J. Botineau, "Observation of dissipative superluminous solitons in a brillouin fiber ring laser", *Physical Review Letters*, vol. 66, no. 11, pp. 1454–1457, 1991. DOI: `10.1103/physrevlett.66.1454`.

[61] E. V. Vanin, A. I. Korytin, A. M. Sergeev, D. Anderson, M. Lisak, and L. Vázquez, "Dissipative optical solitons", *Physical Review A*, vol. 49, no. 4, pp. 2806–2811, 1994. DOI: `10.1103/physreva.49.2806`.

[62] N. Akhmediev and A. Ankiewicz, "Dissipative solitons in the complex ginzburg-landau and swift-hohenberg equations", in *Dissipative Solitons*, N. Akhmediev and A. Ankiewicz, Eds. Berlin, Heidelberg: Springer Berlin Heidelberg, 2005, pp. 1–17. DOI: `10.1007/10928028_1`.

[63] J. M. Soto-Crespo, N. Akhmediev, and A. Ankiewicz, "Pulsating, creeping, and erupting solitons in dissipative systems", *Physical Review Letters*, vol. 85, no. 14, pp. 2937–2940, 2000. DOI: `10.1103/physrevlett.85.2937`.

[64] N. Akhmediev, J. M. Soto-Crespo, and G. Town, "Pulsating solitons, chaotic solitons, period doubling, and pulse coexistence in mode-locked lasers: Complex ginzburg-landau equation approach", *Physical Review E*, vol. 63, no. 5, 2001. DOI: `10.1103/physreve.63.056602`.

[65] J. Wilson and J. Hawkes, *Optoelectronics: an introduction*, 3rd ed. Prentice Hall, 1998.

[66] L. Dai, Z. Huang, Q. Huang, C. Zhao, A. Rozhin, S. Sergeyev, M. A. Araimi, and C. Mou, "Carbon nanotube mode-locked fiber lasers: Recent progress and perspectives", *Nanophotonics*, vol. 10, no. 2, pp. 749–775, 2020. DOI: `10.1515/nanoph-2020-0446`.

[67] J. N. Kutz, "Mode-locked soliton lasers", *SIAM Review*, vol. 48, no. 4, pp. 629–678, 2006. DOI: `10.1137/s0036144504446357`.

[68] L. Monroy, M. Jiménez-Rodríguez, E. Monroy, M. González-Herráez, and F. B. Naranjo, "High-quality, inn-based, saturable absorbers for ultrafast laser development", *Applied Sciences*, vol. 10, no. 21, 2020. DOI: `10.3390/app10217832`.

[69] J. D. Moores, "On the ginzburg-landau laser mode-locking model with fifth-order saturable absorber term", *Optics Communications*, vol. 96, no. 1-3, pp. 65–70, 1993. DOI: `10.1016/0030-4018(93)90524-9`.

[70] E. Ding and J. N. Kutz, "Operating regimes, split-step modeling, and the haus master mode-locking model", *Journal of the Optical Society of America B*, vol. 26, no. 12, p. 2290, 2009. DOI: `10.1364/josab.26.002290`.

[71] D. D. Morrison, J. D. Riley, and J. F. Zancanaro, "Multiple shooting method for two-point boundary value problems", *Communications of the ACM*, vol. 5, no. 12, pp. 613–614, 1962. DOI: `10.1145/355580.369128`.

[72] J. Yang, "Newton-conjugate-gradient methods for solitary wave computations", *Journal of Computational Physics*, vol. 228, no. 18, pp. 7007–7024, 2009. DOI: `10.1016/j.jcp.2009.06.012`.

[73] J. Yang, "A numerical method for computing time-periodic solutions in dissipative wave systems", *Studies in Applied Mathematics*, vol. 134, no. 4, pp. 420–455, 2015. DOI: `10.1111/sapm.12071`.

[74] J. R. Shewchuk, "An introduction to the conjugate gradient method without the agonizing pain", USA, Tech. Rep., 1994.

[75] J. P. Boyd, "Deleted residuals, the QR-factored newton iteration, and other methods for formally overdetermined determinate discretizations of nonlinear eigenproblems for solitary, cnoidal, and shock waves", *Journal of Computational Physics*, vol. 179, no. 1, pp. 216–237, 2002. DOI: `10.1006/jcph.2002.7052`.

[76] B. Fornberg and G. B. Whitham, "A numerical and theoretical study of certain nonlinear wave phenomena", *Philosophical Transactions of the Royal Society of London. Series A, Mathematical and Physical Sciences*, vol. 289, no. 1361, pp. 373–404, 1978. DOI: `10.1098/rsta.1978.0064`.

[77] J. Butcher, "A history of Runge-Kutta methods", *Applied Numerical Mathematics*, vol. 20, no. 3, pp. 247–260, 1996. DOI: `10.1016/0168-9274(95)00108-5`.

[78] P. Moin, *Fundamentals of Engineering Numerical Analysis*, 2nd ed. Cambridge University Press, 2010.

[79] S. C. Chapra and R. P. Canale, *Numerical Methods for Engineers*, 7th ed. McGraw Hill Education, 2015.

[80] J. Widjaja, E. Kobakhidze, T. R. Cartwright, J. P. Lourdesamy, A. F. J. Runge, T. J. Alexander, and C. M. de Sterke, "Absence of galilean invariance for pure-quartic solitons", *Physical Review A*, vol. 104, no. 4, 2021. DOI: `10.1103/physreva.104.043526`.